Kinematic focus point method for particle mass measurements in missing energy events

Doojin Kim,[a] **Konstantin T. Matchev**[b] **and Prasanth Shyamsundar**[b]

[a]*Department of Physics, University of Arizona,*
Tucson, AZ 85721, U.S.A.

[b]*Institute for Fundamental Theory, Physics Department,*
University of Florida, Gainesville, FL 32611, U.S.A.

E-mail: doojinkim@email.arizona.edu, matchev@ufl.edu,
prasanths@ufl.edu

ABSTRACT: We investigate the solvability of the event kinematics in missing energy events at hadron colliders, as a function of the particle mass ansatz. To be specific, we reconstruct the neutrino momenta in dilepton $t\bar{t}$-like events, without assuming any prior knowledge of the mass spectrum. We identify a class of events, which we call *extreme events*, with the property that the kinematic boundary of their allowed region in mass parameter space passes through the true mass point. We develop techniques for recognizing extreme events in the data and demonstrate that they are abundant in a realistic data sample, due to expected singularities in phase space. We propose a new method for mass measurement whereby we obtain the true values of the mass parameters as the focus point of the kinematic boundaries for *all* events in the data sample. Since the masses are determined from a relatively sharp peak structure (the density of kinematic boundary curves), the method avoids some of the systematic errors associated with other techniques. We show that this new approach is complementary to previously considered methods in the literature where one studies the solvability of the kinematic constraints throughout the mass parameter space. In particular, we identify a problematic direction in mass space of nearly 100% solvability, and then show that the focus point method is effective in lifting the degeneracy.

Contents

1 Introduction

At the Large Hadron Collider (LHC), information about the underlying physics is extracted by studying the kinematic properties of the final state objects (jets, leptons, photons, etc.) which are reconstructed in each collision. Therefore, understanding the unique kinematic features arising from different event topologies is an important step in any LHC data analysis, be it for a new physics search, or a parameter measurement.

For example, the traditional method to discover a new heavy resonance (as well as to measure its mass) is to look for a bump in the invariant mass distribution of its decay products (daughter particles). This procedure is straightforward if the daughter particles are all visible in the detector and their energies and momenta are measured. However, things become more involved if some of the daughter particles are invisible, e.g., they can be neutrinos or new weakly interacting massive particles, as predicted in many models of new physics with dark matter candidates and/or dark sectors [1]. A prime example of this situation is provided by semi-leptonic $t\bar{t}$ events, in which one of the top quarks, say $\bar{t}$, decays hadronically, while the other decays as

$$t \to bW^+ \to b\ell^+\nu, \tag{1.1}$$

where a neutrino ν goes missing. At this point a natural approach would be to attempt to *compute* the momentum of the neutrino from the available kinematic information in the event, perhaps supplemented with some theoretical assumptions. For example, assuming that there are no other invisible particles in the event, we can identify the measured missing transverse momentum $\vec{\not{P}}_T$ in the event with the transverse component $\vec{p}_{\nu T}$ of the neutrino momentum

$$\vec{p}_{\nu T} = \vec{\not{P}}_T. \tag{1.2}$$

On the other hand, the neutrino arises from the decay of a W-boson, which is typically produced on-shell, in turn implying that

$$(p_{\ell^+} + p_\nu)^2 = m_W^2, \tag{1.3}$$

where p_{ℓ^+} and p_ν are the 4-momenta of the lepton and neutrino, respectively, and m_W is the physical mass of the W-boson. Finally, the energy E_ν and 3-momentum $\vec{p}_\nu$ of the neutrino are related by the mass shell condition

$$p_\nu^2 = m_\nu^2, \tag{1.4}$$

where $p_\nu = (E_\nu, \vec{p}_\nu)$. Equations (1.2)–(1.4) provide a total of $2 + 1 + 1 = 4$ constraints on the four components of p_ν, allowing to solve for the neutrino 4-momentum, up to discrete ambiguities.[1] In practice, this is typically done through an eventwise kinematic fit which accounts for the detector resolution and the combinatorial uncertainties [2–4].

Now and for the rest of the paper we shall turn our attention to the much more challenging case of *dilepton* $t\bar{t}$ events, in which *both* top quarks decay leptonically as in (1.1). This event topology is relevant not only for top physics, but also for new physics searches where the decay chains of the newly produced particles terminate in a generic dark matter candidate, i.e., a stable, neutral, weakly interacting particle which is invisible in the detector just like the neutrino. In many such models, e.g., supersymmetry (SUSY) with R-parity [5], universal extra dimensions with KK-parity [6–8], Little Higgs with T-parity [9–12], etc., the

---

[1]The mass constraints (1.3) and (1.4) lead to a quadratic equation, which in general has two solutions. Additional discrete combinatorial ambiguities arise if there are more than one lepton and/or more than one b-jet present in the event.

lifetime of the dark matter particle is protected by an exact Z_2 symmetry, which ensures that new particles are pair-produced at the LHC, leading to symmetric events with two decay chains. From that point of view, dilepton $t\bar{t}$ events are an excellent testbed which allows us to test ideas originally developed for the study of new physics signatures, see, e.g., [13].

Once we consider dilepton $t\bar{t}$ events, we have to face the complication that now there are twice as many unknown momentum components, i.e., the four momenta, p_ν and $p_{\bar{\nu}}$, of the two missing neutrinos. The number of on-shell constraints is also doubled — (1.3) is replaced by

$$(p_{\ell^+} + p_\nu)^2 = m_W^2, \tag{1.5a}$$

$$(p_{\ell^-} + p_{\bar{\nu}})^2 = m_W^2, \tag{1.5b}$$

while (1.4) is replaced by

$$p_\nu^2 = m_\nu^2, \tag{1.6a}$$

$$p_{\bar{\nu}}^2 = m_\nu^2. \tag{1.6b}$$

We also gain a new constraint, that the two parent particles (top quarks) have equal mass:

$$(p_b + p_{\ell^+} + p_\nu)^2 = (p_{\bar{b}} + p_{\ell^-} + p_{\bar{\nu}})^2, \tag{1.7}$$

but the missing transverse momentum constraint (1.2) remains a single 2D vector equation:

$$\vec{p}_{\nu T} + \vec{p}_{\bar{\nu} T} = \vec{\not{P}}_T. \tag{1.8}$$

As a result, the seven constraints (1.5)–(1.8) are not sufficient to determine the eight unknown components p_ν and $p_{\bar{\nu}}$ uniquely, and therefore, one cannot reconstruct the top as a mass bump. The problem is exacerbated in new physics applications, where *a priori* one does not know the masses of the new particles playing the roles of the W-boson and the neutrino, so that the best one can do is to apply the equal mass constraints

$$p_\nu^2 = p_{\bar{\nu}}^2 \tag{1.9}$$

$$(p_{\ell^+} + p_\nu)^2 = (p_{\ell^-} + p_{\bar{\nu}})^2 \tag{1.10}$$

in place of (1.5)–(1.6), leaving us with only 5 constraints (1.7)–(1.10) for 8 unknowns.

There are several possible approaches to tackle this conundrum [14]:

- *Gain additional constraints.* This can be done in several ways. First, one may consider longer decay chains which may occur in new physics scenarios. The classic examples are the three-step squark decay chain and the four-step gluino decay chain in supersymmetry, where the trick of analyzing several events simultaneously could provide the required number of constraints to solve for all unknown momenta, up to discrete ambiguities [15–20]. One may also impose constraints resulting from existing preliminary measurements of the kinematic endpoints of suitable variables [21–23]. Finally, one could preselect a sub-sample of events with special properties, e.g., events located at the kinematic endpoint of a suitable variable, in which case the kinematics of the decays is further constrained [24, 25].

- *Adopt an ansatz for the undetermined components of the invisible momenta.* The idea here is to assign values for the remaining invisible momentum components through a suitable ansatz which preserves some useful property, e.g., that a parent mass bound is not exceeded [26, 27]. Operationally the values are assigned by extremizing some relevant function of the invisible momenta. Often the minimum of the function itself becomes a useful kinematic variable — some well-known examples include the Cambridge M_{T2} variable [28, 29] and its variants [30–33], the $\sqrt{s}_{\min}$ variable [34–36], a variety of constrained transverse mass variables [37–40], the M_{CT2} variable [41, 42], the M_{2C} variable [43, 44], the MAOS method [45–48], the M_2 class of variables [49–56], etc. While this approach has useful practical applications, it still only represents an approximate treatment and does not lead to a mass reconstruction through a bump.

- *Use kinematic endpoints of observable invariant mass distributions.* Another logical possibility is to ignore the invisible momenta altogether and design the analysis entirely in terms of the measured momenta of the reconstructed visible objects in the event. Historically this was the original approach which led to the classic analyses of SUSY mass measurements from kinematic endpoints in invariant mass distributions [57–63]. However, as in the previous case, the method relies on the measurement of kinematic endpoints instead of mass bumps. Endpoint measurements are generally challenging — they may be difficult to extract in the presence of background, their location is rather sensitive to the effects of particle widths and detector resolution, and they require fitting to a suitable profile [64, 65], which introduces additional systematics.

- *Check the solvability of an enlarged set of kinematic constraints.* Here the idea is first to enlarge the existing set of kinematic constraints by assuming test values for the unknown masses, and then instead of focusing on the actual solutions for the invisible momenta, simply ask the question whether such solutions exist or not. If solutions do not exist, the corresponding test ansatz for the particle masses is inconsistent with the kinematics of the particular event and those masses are disfavored [16, 17, 66]. By repeating the procedure over the full event sample, one can gradually restrict the allowed mass parameter space, hopefully until it shrinks to a point.[2] Indeed, the true masses should be compatible with every signal event, while for any wrong choice of particle masses, one would hope that, given sufficient statistics, there would be at least one signal event in the data which would have incompatible kinematics. We will illustrate these ideas more explicitly later on in sections 3 and 4. For now we just mention that this method appears to have the desired property that the true particle masses are revealed by a bump in mass parameter space (for example, when plotting the fraction of compatible events). However, as we shall show in section 4, this expectation is misleading, as there is generally a whole "flat direction" of near 100% solvability in mass parameter space.

---

[2] A variant of this technique assigns weights derived from the parton distribution functions to different points in the allowed region of mass parameter space in order to arrive at the most likely value of the particle masses [67].

In this paper we present a new approach to measuring masses in events with $\vec{P}_T$, by building up on the solvability method discussed in the last bullet above. Our method makes crucial use of the singularities in the phase space density which arise from projecting the full phase space of final state momenta into the visible phase space [68]. This method, which we shall call the "kinematic focus points method",[3] has similarities to a traditional mass-bump search in the sense that the density of an appropriately defined quantity will peak at the true values of the unknown masses in the event topology. Previous attempts to design an analysis for measuring the unknown masses in SUSY-like events with missing energy from such bump-like features were limited to the case of a single decay chain [71–75]. Instead, here we will be interested in the more typical situation of two symmetric decay chains. While our method is applicable more generally, we shall introduce it in the context of the dilepton $t\bar{t}$ event topology discussed above.

The paper is organized as follows. In section 2 we specify the process under study, introduce our conventions and terminology, and provide some details on our simulations. In section 3 we list the kinematic constraints for our event topology, and briefly review the idea of using their solvability in order to perform mass measurements (or at the very least, to restrict the allowed region of mass parameter space). In section 4 we discuss the expected outcome from this approach and highlight its advantages as well as potential pitfalls. In particular, we identify a flat direction in mass parameter space of nearly 100% solvability, along which the masses are consistent with the kinematics of nearly all events in the data. We then show that by performing complementary measurements of kinematic endpoints one is able to lift the flat direction and identify the true mass point.[4]

In the remaining sections, we define the kinematic focus point method and illustrate its performance. First in section 5 we discuss the event-wise kinematic boundaries in mass parameter space, and introduce the notion of "extreme" events, i.e., events for which the kinematic boundary passes through the true mass point. We argue that extreme or near-extreme events are quite abundant in a realistic data sample. More importantly, we show that the density of extremeness boundaries in the mass parameter space is singular at the true mass point.[5] Using the results from section 5, in section 6 we motivate the kinematic focus points method and proceed to investigate its performance for two cases — a SUSY-like mass spectrum (where top events are part of the SM background) as well as for top pair-production itself, thus allowing for a measurement of the top, W-boson and neutrino masses independently.[6] In section 7, we present our conclusions and outlook for future studies. In appendix A we derive the parametric equation for the flat direction of low mass sensitivity encountered in sections 4 and 6.

---

[3]Not to be confused with the focus point phenomenon in the RGE running of certain SUSY mass parameters [69, 70].

[4]To the careful reader, this should not come as a surprise, since kinematic endpoint measurements by themselves are already able to fully determine the mass spectrum [13, 30].

[5]This is a purely mathematical statement which is valid in the zero width approximation and in the absence of detector smearing. Both of those effects will lead to some smearing of the singularity, the extent of which is studied later on in sections 6.4 and 6.5.

[6]An analogous procedure based on kinematic endpoints was advertised in [30] and tested in [13].
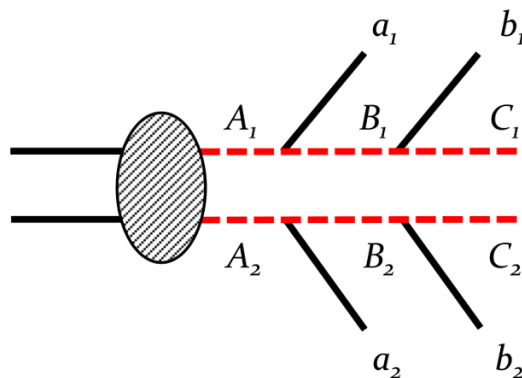
Figure 1. A schematic depiction of the dilepton $t\bar{t}$ event topology. Two heavy particles, A_1 and A_2, are pair-produced, and each A_i decays via two successive two-body decays as $A_i \rightarrow a_i B_i \rightarrow a_i b_i C_i$. In general, A_i, B_i and C_i are new particles of *a priori* unknown masses. The two branches are assumed to be identical and the intermediate resonances A_i and B_i are assumed to be on-shell. The final state particles a_i and b_i are visible Standard Model particles which for simplicity will be assumed massless throughout the analysis. The final state particles C_i are invisible in the detector and their momenta are not measured.

2 Notations and setup

2.1 Conventions

In this paper, we consider the $t\bar{t}$-like event topology depicted in figure 1. A pair of heavy particles, A_1 and A_2, is initially produced, and each A_i decays via two successive two-body decays:

$$pp \rightarrow A_1 A_2, \tag{2.1a}$$

$$A_i \rightarrow a_i B_i \rightarrow a_i b_i C_i \quad (i = 1, 2), \tag{2.1b}$$

to two visible Standard Model particles a_i and b_i and an invisible particle C_i. The two branches in figure 1 are assumed to be identical and the intermediate resonances A_i and B_i will be taken to be on-shell. The true masses of particles A_i, B_i and C_i are *a priori* unknown, and will be denoted by m_A, m_B and m_C, respectively. The goal is to measure m_A, m_B and m_C independently from a sample of events with the topology of figure 1.

Since the final state particles a_i and b_i are visible in the detector, their 4-momenta, p_{a_i} and p_{b_i}, are measured known quantities for each event. In many new physics models with this event topology, a_i and b_i are bottom quarks and leptons, respectively, just like the case of dilepton $t\bar{t}$ events. Then, the a's can be distinguished from the b's, but there remains a twofold ambiguity in partitioning the two a's and the two b's into the two branches. As there are already several suggestions in the literature on how to address this combinatorial issue [76–78], we shall not dwell on the combinatorial problem any further. Note that our proposed method below will be robust against combinatorial issues, since it will rely on detecting a peak structure which is absent from the combinatorial background. Therefore, for clarity of the presentation, in what follows we shall assume that the visible particles have been properly assigned to the two branches.

The final state particles C_i are invisible in the detector (C is typically a dark matter candidate). Consequently, their 4-momenta, q_i, are *a priori* unknown. The 4-momenta of B_i and A_i are denoted by $q_{B_i}(\equiv p_{b_i} + q_i)$ and $q_{A_i}(\equiv p_{a_i} + p_{b_i} + q_i)$, respectively. Note that the notation here follows that of [26], where the letter p is used to denote known momenta, while q is used for *a priori* unknown momenta. An overhead arrow will be used to denote the spatial component $\vec{p}$ of a 4-momentum p. The beam axis (the longitudinal direction) is chosen to be the z axis, while the transverse components of a 4-momentum p will be denoted by $\vec{p}_T$. The product of two 4-momenta will refer to their Lorentz inner product.

We shall often consider hypothesized values for the *a priori* unknown masses, i.e., *test* or *trial* masses, which will be denoted by a tilde: $\tilde{m}_A$, $\tilde{m}_B$, and $\tilde{m}_C$. For convenience, the singular form *true mass* and *test mass* will sometimes be used to refer to a set of true masses (m_A, m_B, m_C) and a set of test masses $(\tilde{m}_A, \tilde{m}_B, \tilde{m}_C)$. For notational convenience, q_i, q_{B_i} and q_{A_i} will be used interchangeably as variables or particular values for these variables, and the meaning will be clear from the context.

2.2 Simulation details

The analyses in this study were performed on events generated as follows.

- Obviously, the event topology of figure 1 can be applied directly to the study of top quark pair production, in which case the particles A, B and C are the top quark, the W-boson and the neutrino, respectively. While their masses m_t, m_W and m_ν, are already known, the techniques discussed below can still be used to perform more sensitive measurements of those SM parameters. Our primary target, however, is a new physics event topology of the type shown in figure 1, where the three masses m_A, m_B and m_C are *a priori* unknown. For example, in SUSY A can be a top squark, B a chargino and C a sneutrino. Thus for our main simulation we choose a study point with a spectrum of $m_A = 1000$ GeV, $m_B = 800$ GeV and $m_C = 700$ GeV. Note that the mass differences are relatively modest, so that the p_T and energy distributions of the jets and leptons in the signal are similar to those of the main background (dilepton $t\bar{t}$ events), so that a template-matching method is unlikely to be very sensitive.

- For clarity of the presentation, the resonances A_i and B_i were kept on-shell. Including small widths for these particles will lead to a slight smearing of the peaks and endpoints discussed in the study [79, 80].

- The visible final state particles a_i and b_i were taken to be massless. This is a very good approximation in the typical scenario where a_i and b_i are bottom quarks and leptons, respectively. Regardless, the mass measurement methods considered here do not rely on this choice, and this assumption can be easily relaxed if needed.

- For definiteness the decay vertices were taken to be non-chiral, i.e., there are no non-trivial spin effects. This assumption also does not impact our results, since the methods studied below are based on purely kinematics arguments and are therefore model independent.

- The parent particles A_i were pair produced at LHC center of mass energy of 13 TeV. For simplicity, initial state radiation (ISR) was not turned on. Again, this assumption has little bearing on our results — for example the ISR jets are unlikely to be b jets in which case one might worry that they can be confused with particles a_i in figure 1, complicating the combinatorial issue.

- The events were generated at the parton level with MADGRAPH [81] and resonances were decayed by phase space. Initially, we will show results with no detector simulation applied, before studying the effects of the detector resolution in sections 6.4 and 6.5.

3   Solvability of kinematic constraints

The general problem with missing energy events is that there exist final state momenta (q_i in our case) which are not measured. However, if we could somehow *calculate* the invisible momenta q_i (and from there q_{B_i} and q_{A_i}), the unknown masses can be simply obtained by $m_A^2 = q_{A_i}^2$, $m_B^2 = q_{B_i}^2$ and $m_C^2 = q_i^2$. This motivates us to study the kinematic constraints obeyed by the invisible momenta.

With the notation from section 2, the five kinematic constraints (1.7)–(1.10) for the event topology in figure 1 become

$$q_1^2 = q_2^2 \tag{3.1a}$$

$$(p_{b_1} + q_1)^2 = (p_{b_2} + q_2)^2 \tag{3.1b}$$

$$(p_{a_1} + p_{b_1} + q_1)^2 = (p_{a_2} + p_{b_2} + q_2)^2 \tag{3.1c}$$

$$\vec{q}_{1T} + \vec{q}_{2T} = \vec{\mathcal{P}}_T \tag{3.2}$$

These five constraints are clearly insufficient to determine all 8 unknown components of q_i. To this end, we introduce test masses $(\tilde{m}_A, \tilde{m}_B, \tilde{m}_C)$ with $\tilde{m}_A > \tilde{m}_B > \tilde{m}_C$. The constraints in eq. (3.1) are thus enlarged to

$$q_1^2 = \tilde{m}_C^2, \tag{3.3a}$$

$$q_2^2 = \tilde{m}_C^2 \tag{3.3b}$$

$$(p_{b_1} + q_1)^2 = \tilde{m}_B^2 \tag{3.3c}$$

$$(p_{b_2} + q_2)^2 = \tilde{m}_B^2 \tag{3.3d}$$

$$(p_{a_1} + p_{b_1} + q_1)^2 = \tilde{m}_A^2 \tag{3.3e}$$

$$(p_{a_2} + p_{b_2} + q_2)^2 = \tilde{m}_A^2 \tag{3.3f}$$

Together with eq. (3.2), these six constraints make up a total of 8 kinematic constraints which can be solved by standard means [82–84] in order to yield test values for the unknown momenta q_i corresponding to the given choice of test masses $(\tilde{m}_A, \tilde{m}_B, \tilde{m}_C)$.

At this point it might seem that we have not made much progress, since we have traded one set of unknowns for another. The key idea now is to focus not on the actual solutions
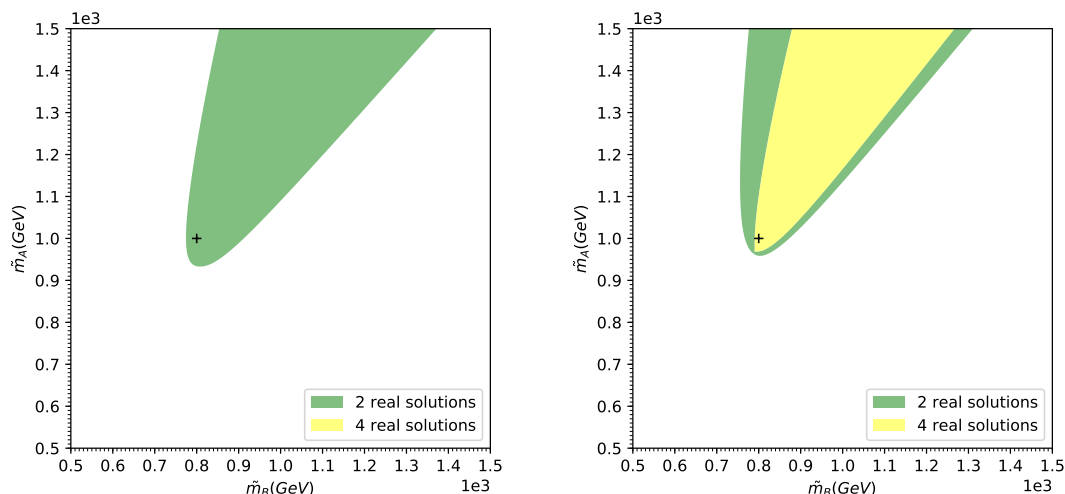
Figure 2. Solvability plots for two different events, showing the number of solutions allowed by different values of $(\tilde{m}_B, \tilde{m}_A)$. The test mass $\tilde{m}_C$ has been fixed to be the true mass, $\tilde{m}_C = m_C = 700$ GeV. Uncolored areas in the plots correspond to zero real solutions, while green (yellow) regions correspond to two (four) solutions. The cross marks the true mass point (m_B, m_A). For the event on the left, the plot only shows an allowed region with 2 real solutions (the allowed region with four solutions is outside the plot range). For the event on the right, both a region with 2 solutions and a region with 4 solutions can be seen.

for the invisible momenta, but on the existence (or lack thereof) of viable solutions in the first place [16, 17, 66]. Indeed, not all choices of test masses will lead to real solutions for q_i. In general, the kinematic constraints (3.2) and (3.3) allow four complex solutions. Non-real solutions come in complex conjugate pairs [3], and therefore, there can be either zero, two or four real (possibly degenerate) solutions for a given test mass. As a result, each event separates the three-dimensional mass parameter space $(\tilde{m}_A, \tilde{m}_B, \tilde{m}_C)$ into *allowed* and *disallowed* regions, depending on whether there exists a real solution for q_i or not. The event will be said to be *solvable* by the test mass if there exists a real solution for q_i. Note that for signal events the true mass point will always solve the event,[7] and thus can never be ruled out.

Figures 2–4 illustrate the above discussion for two representative signal events. In the figures, we show '"solvability plots" constructed as follows. Given that it is difficult to visualize the full three-dimensional mass parameter space, we choose to present slices at fixed values of $\tilde{m}_C$: in figure 2 $\tilde{m}_C$ is set to the true value of $m_C = 700$ GeV, while in figure 3 we take $\tilde{m}_C = 600$ GeV and in figure 4 we have $\tilde{m}_C = 800$ GeV. In each panel, we color-code the $(\tilde{m}_B, \tilde{m}_A)$ plane according to the number of real solutions to the kinematic constraints (3.2) and (3.3): white (uncolored) areas correspond to no real solutions, green areas have two real solutions and yellow areas allow four real solutions. The cross in figure 2 marks the true mass point $m_B = 800$ GeV, $m_A = 1000$ GeV (the cross is absent in figures 3 and 4 since the test mass $\tilde{m}_C$ in those figures is different from the true value m_C).

---

[7]Barring the effects from the detector resolution and finite particle widths.
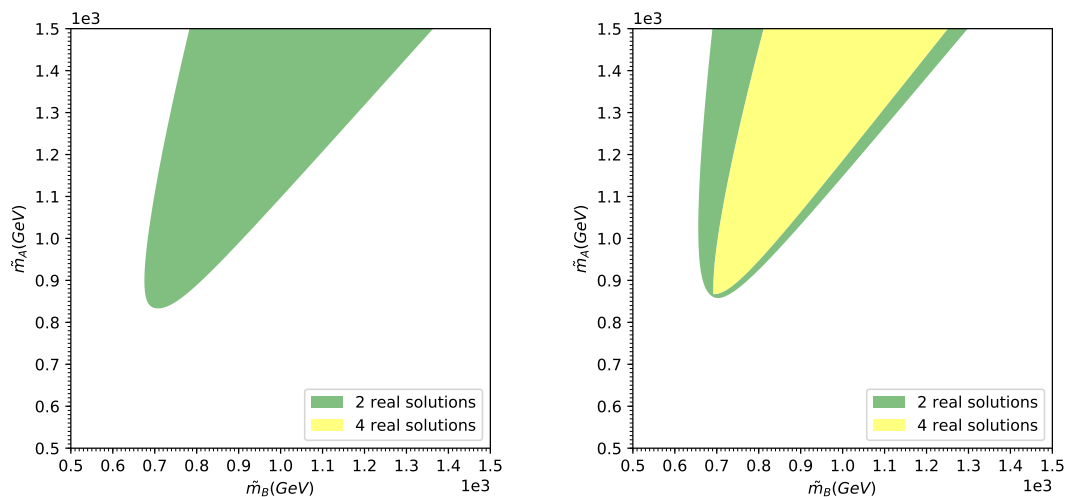
Figure 3. The same as figure 2, except the trial mass $\tilde{m}_C$ is now chosen to be smaller than the true mass: $\tilde{m}_C = 600\,\text{GeV} < m_C$. Since $\tilde{m}_C$ is different from m_C, the true mass point is not seen in these plots.
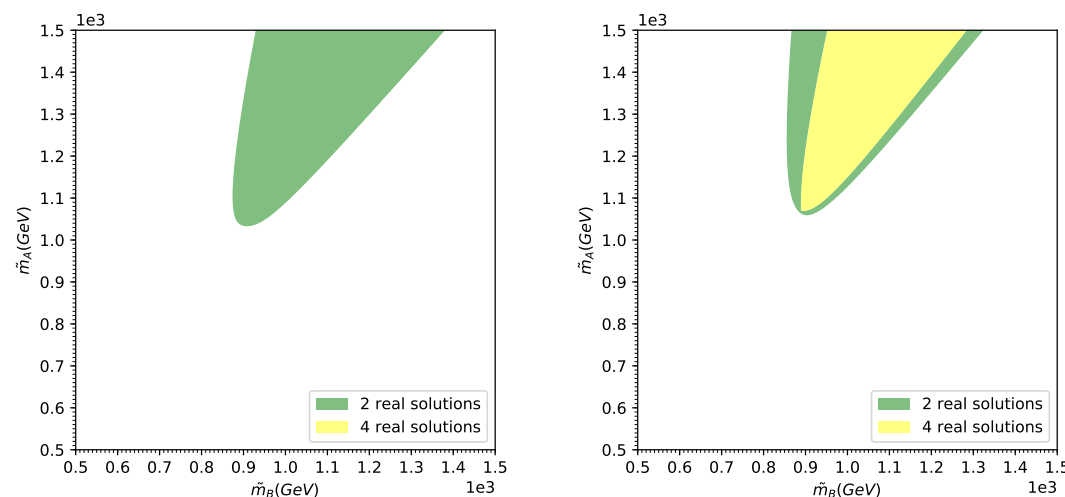

Figure 4. The same as figure 3, but for a choice of test mass $\tilde{m}_C$ larger than the true mass: $\tilde{m}_C = 800\,\text{GeV} > m_C$.

There are several important lessons which can be learned from these figures. First, it is rather remarkable that the large majority of the plotted areas are actually ruled out by this single event — notice how the white color is the dominant one on the plots. We also observe that as the third (fixed) test mass $\tilde{m}_C$ is decreased (increased), the allowed region in the $(\tilde{m}_B, \tilde{m}_A)$ plane correspondingly shifts towards lower (higher) values of $\tilde{m}_B$ and $\tilde{m}_A$. In turn, the allowed region itself has two sub-regions, with 2 and 4 real solutions, correspondingly. The (yellow-colored) region with 4 real solutions sometimes appears at relatively large masses, and this just happens to be the case with the event used for the left panels in figures 2–4. Finally, it is worth noting that for both of these randomly chosen events, the true mass point marked with the cross in figure 2 is located rather close to the

boundary of the allowed region. At this point, this may seem to be just a coincidence, but a more extensive search throughout the signal event sample reveals that this property is actually quite generic. This observation then brings up the question whether it is possible for the true mass point to be located *exactly* on the boundary of the allowed region. This is one of the central issues in this paper, which will be addressed below in section 5. But first we shall present and discuss the mass measurement method based on solvability.

4 Solvability as a mass measurement method

4.1 Superposition of individual events

In the previous section, we saw that by requiring solvability, a single event can already rule out a sizable chunk of the three-dimensional mass parameter space $(\tilde{m}_A, \tilde{m}_B, \tilde{m}_C)$. Repeating the same analysis with a different event, we would expect a slightly different portion of the mass space to be disfavored. Then, by taking the intersection of the two regions allowed by the individual events, we will further constrain the mass parameter space [16, 17, 66, 71].

This procedure is pictorially illustrated in figure 5, where we use the same two events as in figures 2–4 above. In the top row, we replot the result from figure 2 for $\tilde{m}_C = m_C =$ 700 GeV, only now we remove the distinction between the green and yellow regions (with 2 and 4 real solutions, respectively) and uniformly shade the allowed region in light blue. Then in the plot shown in the bottom row, we superimpose these two allowed regions, thus obtaining a new partition of the $(\tilde{m}_B, \tilde{m}_A)$ plane into three possible regions: where neither event is solvable (white areas), where only one of the events is solvable but not the other (light blue areas) and where both events are solvable (dark blue areas). By construction, the dark blue region where both events are solvable is smaller than each of the individual allowed regions seen in the plots in the top row. This demonstrates the benefit from adding more events to the discussion, i.e., increasing the statistics. At the same time, a pessimist might point out that a) the benefit does not seem to be that great, since the improvement (the light blue areas in the bottom panel of figure 5) is relatively minor when compared to the overall size of the remaining allowed region (the dark blue area); and b) that the remaining dark blue allowed region still seems to extend out to infinity in the "northeast" direction. A crucial question, therefore, becomes how much further the allowed region will shrink once we add all of our remaining events in the data sample. We will answer this question in the next two subsections 4.2 and 4.3, where for clarity of the presentation we split the discussion into two parts: in section 4.2 we focus on the issue of measuring m_A and m_B for a given value of $\tilde{m}_C$ (which throughout that subsection will be fixed to be the true mass m_C) and then in section 4.3 we shall tackle the question of measuring m_C itself. The reason for this separation is twofold: first, it is difficult to present and visualize our results in the full three-dimensional mass parameter space $(\tilde{m}_A, \tilde{m}_B, \tilde{m}_C)$, and second, as we shall see below, the three-dimensional mass parameter space exhibits a direction of relatively low sensitivity, which can be parametrized by the value of $\tilde{m}_C$ (see appendix A for details). As a result, the measurement of m_C will turn out to be much more challenging than the measurements of m_A and m_B.
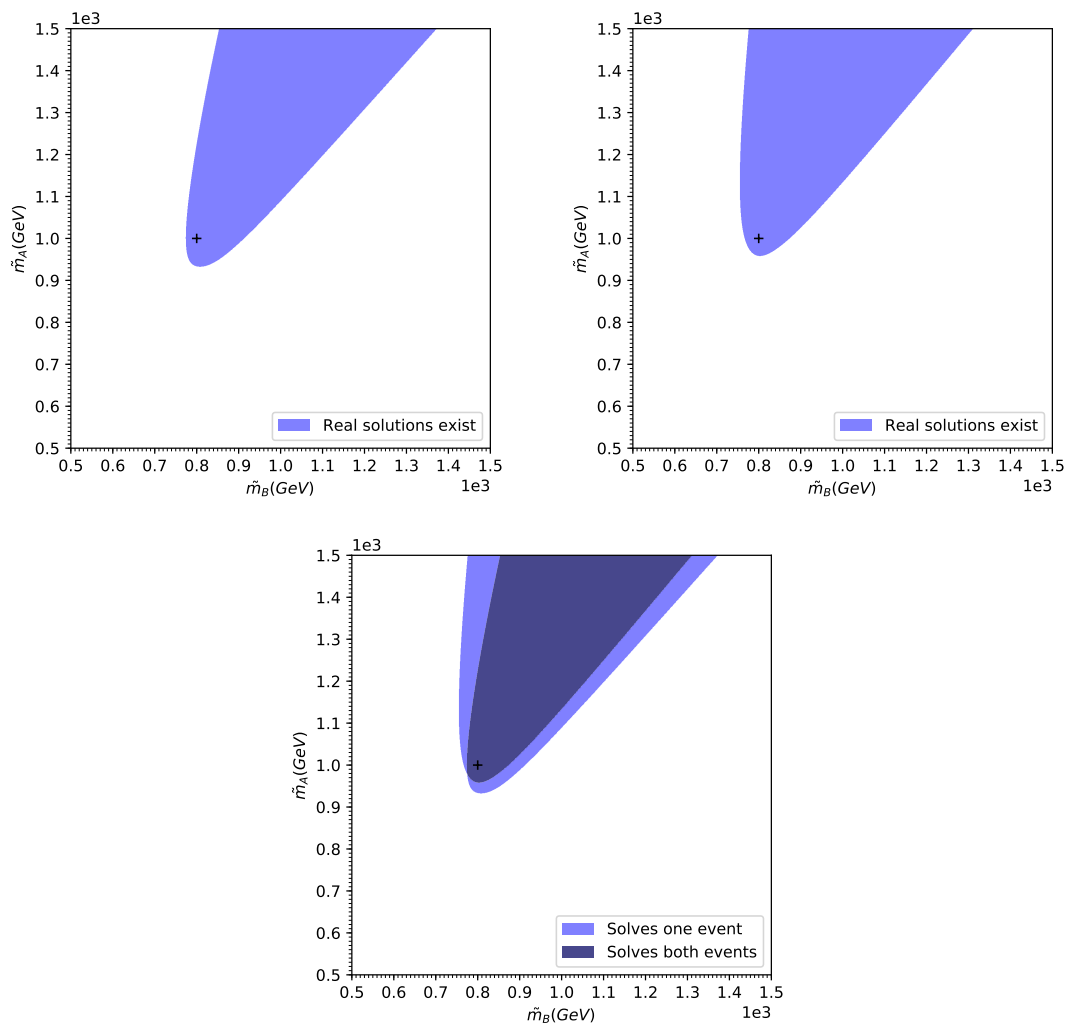
Figure 5. Top row: the same as figure 2 ($\tilde{m}_C = m_C = 700$ GeV), only now the allowed region is uniformly shaded (in light blue), regardless of the number of real solutions. Bottom row: superposition of the allowed regions from the two events. White areas are incompatible with both events, light-shaded areas solve one event but not the other, while the dark-shaded area solves both events.

However, before proceeding to show results with the full event sample, it is useful to consider one more simple exercise, illustrated in figure 6, where we repeat the superposition of allowed regions done in figure 5, still with just a handful of events, in this case three. The important new twist here is that the three events in figure 6 were not chosen at random, as was done in figure 5, but were more carefully selected. The idea was to pick events which are maximally incompatible with each other, and would therefore rule out the largest amount of mass space by themselves. The top left, top right and bottom left panels in figure 6 show the allowed regions for the three selected events. There are three notable features of these individual allowed regions.

- For all three events, the cross marking the true mass point (m_B, m_A) lies on the boundary of the allowed region. This answers the question posed towards the end
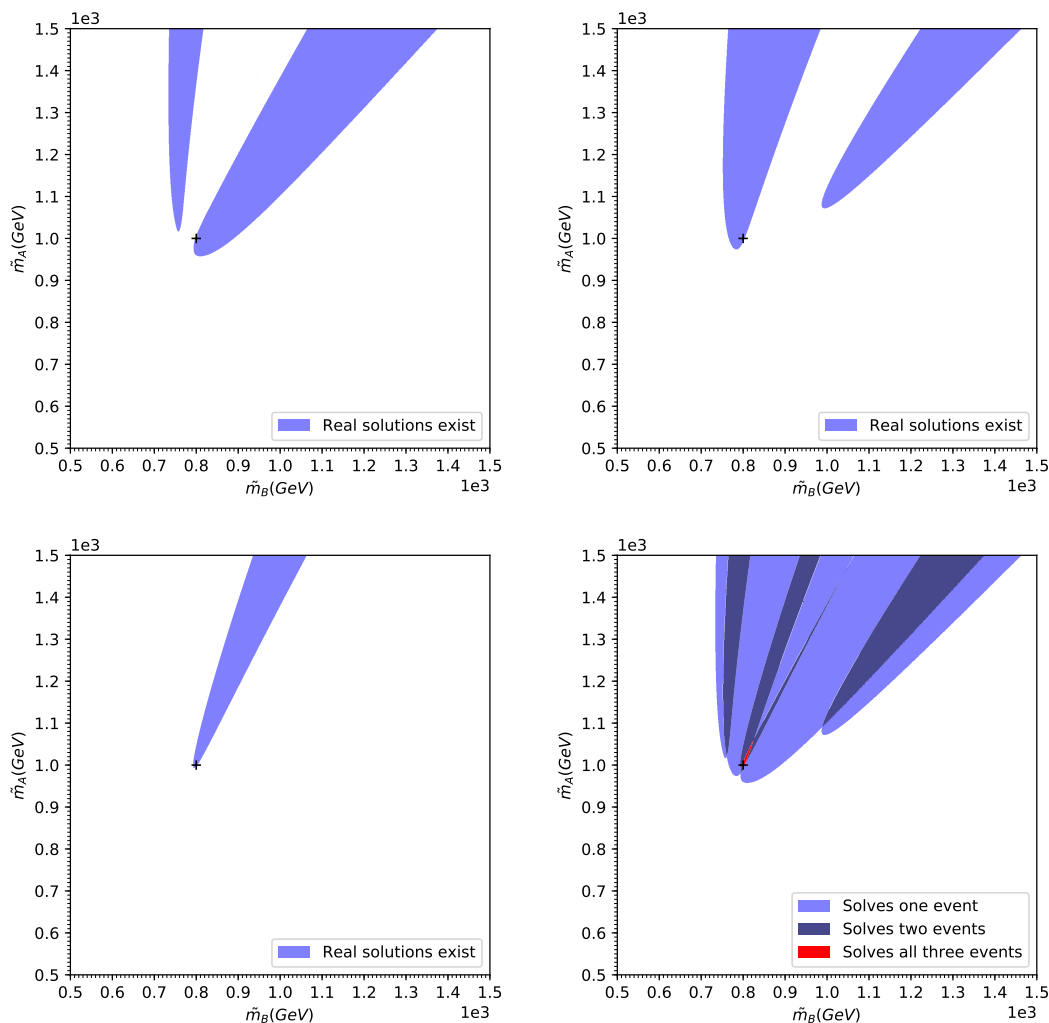
Figure 6. The same as figure 5, only now we superimpose the allowed regions for three suitably chosen events (shown in the top left, top right and bottom left panels). The cross marks the true mass point (m_B, m_A). The three events were selected to be complementary to each other in the sense that when taken together they would rule out a large portion of the parameter space. In the bottom right panel white areas are incompatible with all three events, blue light-shaded areas solve one event but not the other two, blue dark-shaded areas solve two events, but not the third, while the narrow red-shaded sliver extending away from the cross solves all three events.

of the previous section, demonstrating that a kinematic boundary may pass through the true mass point. We shall have a lot more to say about that in the next section 5.

- The shapes of the three allowed regions are very different. For the events in the top row, we see the appearance of two apparently disjoint branches — however, those are actually connected to each other at large values of $\tilde{m}_B$ and $\tilde{m}_A$ beyond the plot range.

- More importantly, the locations of the individual allowed regions happen to be different, so that when they are superimposed in the bottom right panel, there is only a very narrow sliver of allowed mass space left (the red-shaded area). Note the dif-

ferent location of the cross (the true mass point) for the three events: in the top left (top right) panel the cross is on the upper (lower) boundary of the allowed region, so that when the two events are superimposed, they will leave only the "southwest-to-northeast" direction as viable. On the other hand, the cross in the lower left panel is right at the tip of the allowed region, thus eliminating the "southwest" portion, and leaving only the red-shaded area extending to the northeast of the true mass point.

The lesson from figures 5 and 6 is that some events are better at ruling out mass parameter space than others. Unfortunately, since *a priori* we do not know the values of the true masses, i.e., the location of the cross in figures 5 and 6, we are unable to preselect events which are "good at" eliminating parameter space, and the best we can do is go over the whole sample, thus guaranteeing ourselves that at some point we will eventually hit on some "good" events as well. This is precisely what we intend to do in the next two subsections.

4.2 Measuring m_B and m_A for a given trial mass $\tilde{m}_C$

In this subsection we focus on a slice of the three-dimensional mass parameter space $(\tilde{m}_A, \tilde{m}_B, \tilde{m}_C)$ at a constant $\tilde{m}_C$, i.e., we shall attempt to measure the values of m_B and m_A given a value for $\tilde{m}_C$, which we shall take to be the true mass, m_C. However, this choice is inconsequential, and the results will be similar for any other choice of $\tilde{m}_C$ (in the next subsection we shall return to the question of measuring m_C itself).

To this end, we follow the procedure illustrated in figures 5 and 6, only this time we use the full event sample. With realistic detector resolutions and finite widths for the resonances, even the true mass point is not expected to solve 100% of the events. Its success rate will be further reduced in the presence of background events. So, instead of successively restricting the allowed mass space with more and more events, which would eventually result in an empty set, a better approach is to look at the fraction of events that are solvable by a given test mass hypothesis, with the hope that the true test mass exhibits the highest such fraction. The result[8] is plotted in figure 7, where we use only signal events and for now ignore the effects of detector resolution and finite particle widths. The color represents the fraction of events which are solvable for the given mass hypothesis $(\tilde{m}_A, \tilde{m}_B)$.

Figure 7 confirms that, as expected, the true mass point $m_B = 800$ GeV and $m_A = 1000$ GeV has a 100% solvability rate. However, in addition to the true mass point, there also seems to be a whole line of masses with nearly 100% solvability. This "solvability flat direction" is precisely the northeast-pointing red-shaded region previously encountered in figure 6. What we are now finding in figure 7 is that this problematic region persists even after considering the full statistics in the sample. This certainly presents a problem — it suggests that in its current form the solvability method cannot uniquely determine the masses, even in this simplified exercise where we only look at the two-dimensional $(\tilde{m}_B, \tilde{m}_A)$ plane.

One can think of several possible ways out. Perhaps the flat direction seen in figure 7 is not exactly flat, but has a gentle slope, which would nevertheless pick out the true masses.

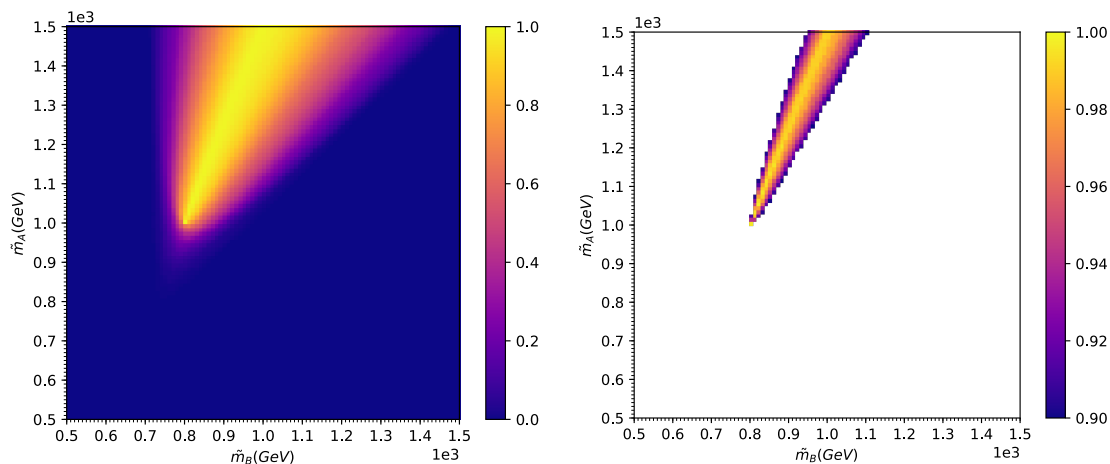[8]From now on such plots will be referred to as "solvability heat maps".

Figure 7. Solvability heat maps for fixed $\tilde{m}_C = m_C = 700$ GeV. For each point in the $(\tilde{m}_A, \tilde{m}_B)$ plane we show the fraction of events which are solvable. The plot on the right considers only mass points which solve over 90% of the events (note the change of scale in the colorbar).

To test this, in the right panel of figure 7 we change the color scale, zooming in on the events with maximal solvability (above 90%). We observe that the problematic direction is still pretty flat, and any existing gentle slope will be washed out once we add the realistic effects of detector resolution and backgrounds.[9] We conclude that for any practical purposes the "solvability flat direction" is there, and we need additional information in order to lift this degeneracy.

For example, we can augment the solvability method with constraints on the masses from kinematic endpoint measurements. The available measurements for this topology are [30]:

$$\{M_{T2}^{\max}(ab), M_{T2}^{\max}(a), M_{T2}^{\max}(b), m_{ab}^{\max}\}. \tag{4.1}$$

The first three are the upper kinematic endpoints for the three possible subsystem M_{T2} variables in the event topology of figure 1, where we have used the notation of ref. [50]. The last one is the upper kinematic endpoint in the distribution of the invariant mass of a_i and b_i. The measurement of any one of these endpoints acts as an additional constraint on the masses. In particular, figure 8 shows the effect of each individual kinematic endpoint measurement on the $(\tilde{m}_B, \tilde{m}_A)$ parameter space from figure 7. Since $\tilde{m}_C$ is still fixed at $\tilde{m}_C = m_C = 700$ GeV, each kinematic endpoint measurement leads to a relation among $\tilde{m}_B$ and $\tilde{m}_A$ as given by the corresponding colored curve: blue for $M_{T2}^{\max}(ab)$, orange for $M_{T2}^{\max}(a)$, green for $M_{T2}^{\max}(b)$, and red for $m_{ab}^{\max}$. We see that all four curves intersect at the true mass point (m_B, m_A), as they should. More importantly, neither of the four curves is aligned with the solvability flat direction, and consequently, any one of them can be used for lifting the degeneracy. We thus conclude that the solvability method is able to

---

[9]The careful reader will note that the flat direction appears to terminate at the true mass point, so that the true mass point is given not by the condition of maximal solvability, but by the sudden drop in the solvability rate along the flat direction. This conjecture is correct [66] and can be further motivated by ideas from sections 5 and 6 below.
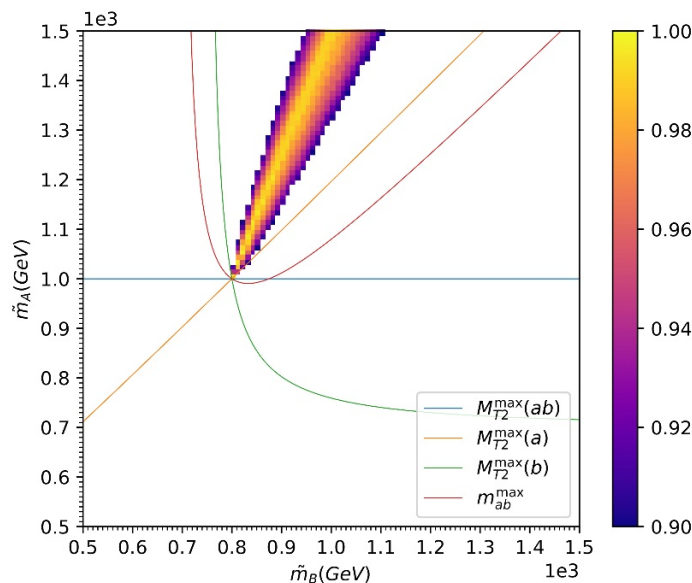
Figure 8. Solvability heat map and constraints from measuring the kinematic endpoints (4.1): $M_{T2}^{\max}(ab)$ (blue), $M_{T2}^{\max}(a)$ (orange), $M_{T2}^{\max}(b)$ (green) and $m_{ab}^{\max}$ (red).

pinpoint the correct mass values in the $(\tilde{m}_B, \tilde{m}_A)$ plane (at fixed $\tilde{m}_C = m_C$), but only when supplemented with a kinematic endpoint measurement.

4.3 Measuring m_C

We now turn our attention to determining m_C. We begin by recreating the solvability heat maps from figure 7 in section 4.2, only this time we choose different values of the trial mass parameter $\tilde{m}_C$, away from the true value $m_C = 700$ GeV. Results for $\tilde{m}_C = 600$ GeV and $\tilde{m}_C = 800$ GeV are shown in figures 9 and 10, respectively. They confirm the trend observed in figures 2–4, namely, that as we increase (decrease) the value of $\tilde{m}_C$, the preferred values of $\tilde{m}_B$ and $\tilde{m}_A$ increase (decrease) as well. Unfortunately, the solvability heat maps in figures 9 and 10 look qualitatively very similar to the heat map in figure 7 for $\tilde{m}_C = m_C$. Therefore, it appears very difficult to extract the correct value of m_C solely on the basis of these two-dimensional heat maps in the $(\tilde{m}_B, \tilde{m}_A)$ plane; some additional input is needed.

The measurements of the kinematic endpoints (4.1) might just be this missing input. Figure 8 demonstrated that with the correct value of $\tilde{m}_C$, the measurements (4.1) are consistent among themselves, as well as with the solvability heat map. It is worth checking whether this consistency is retained when we use erroneous values of $\tilde{m}_C$, i.e., values away from the true mass. This test is performed in figure 11, which shows analogues of figure 8 for $\tilde{m}_C = 400$ GeV (upper left panel), $\tilde{m}_C = 600$ GeV (upper right panel), $\tilde{m}_C = 800$ GeV (lower left panel) and $\tilde{m}_C = 1000$ GeV (lower right panel).

There are several interesting features present in figure 11. First, we note that the blue, orange and green curves corresponding to the three M_{T2} kinematic endpoints always cross at a single point, and therefore the three M_{T2} measurements are consistent with each other, regardless of the chosen value of $\tilde{m}_C$. This is due to the fact that these measurements are
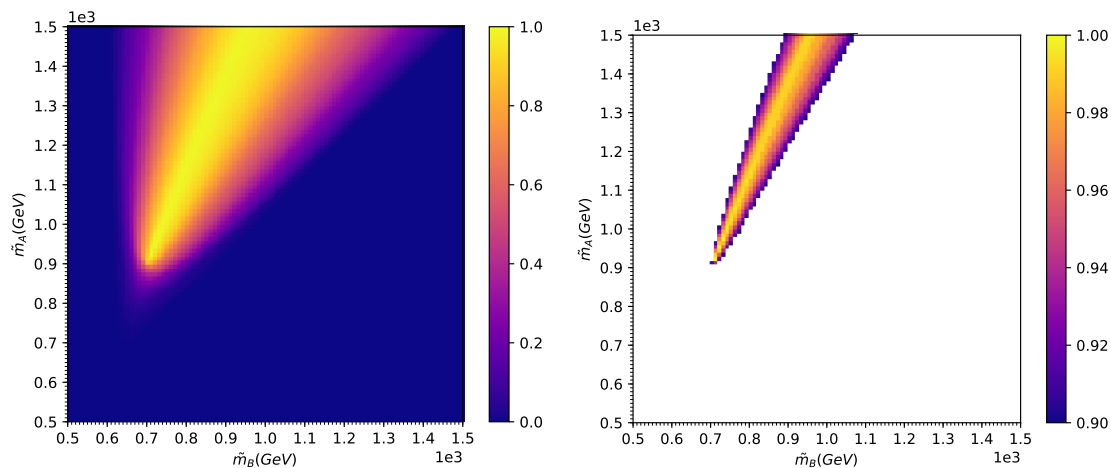
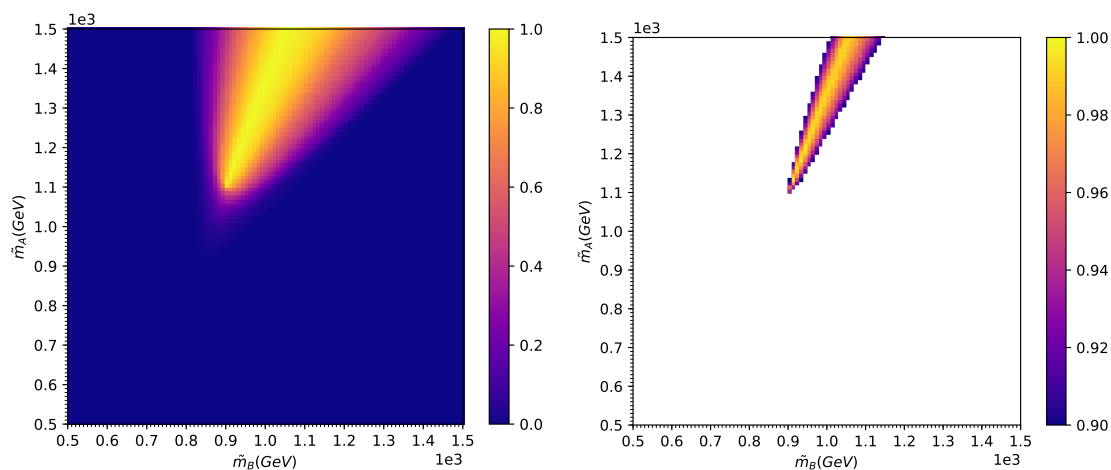**Figure 9**. Solvability heat maps as in figure 7, except here $\tilde{m}_C = 600$ GeV $< m_C$.

Figure 10. Solvability heat maps as in figure 7, except here $\tilde{m}_C = 800$ GeV $> m_C$.

not independent, but obey the relation [30]

$$\left[M_{T2}^{\max}(b)\right]^2 = M_{T2}^{\max}(ab)\left[M_{T2}^{\max}(ab) - M_{T2}^{\max}(a)\right], \tag{4.2}$$

which is in fact why the fourth measurement of $m_{ab}^{\max}$ needed to be added to the set (4.1). On the other hand, the red curve corresponding to the invariant mass endpoint $m_{ab}^{\max}$ is *not* consistent with the others, as it always misses the common crossing point for the three M_{T2} measurements, which is an indication that the chosen value for $\tilde{m}_C$ was incorrect. The mismatch grows as $\tilde{m}_C$ moves further and further away from the true value m_C.

Figure 11 also reveals a discrepancy between the high solvability region, on the one hand, and the various kinematic endpoint measurements, on the other. In particular, at the lower values of $\tilde{m}_C$ below the true mass m_C, the red curve for $m_{ab}^{\max}$ tends to miss the solvable region, while for values of $\tilde{m}_C$ which are too high, it is the blue $M_{T2}^{\max}(ab)$ curve which fails to come into contact with the high solvability region. Therefore, by plotting the maximum fraction of solvable events *along* these constraint curves in the $(\tilde{m}_B, \tilde{m}_A)$ plane,
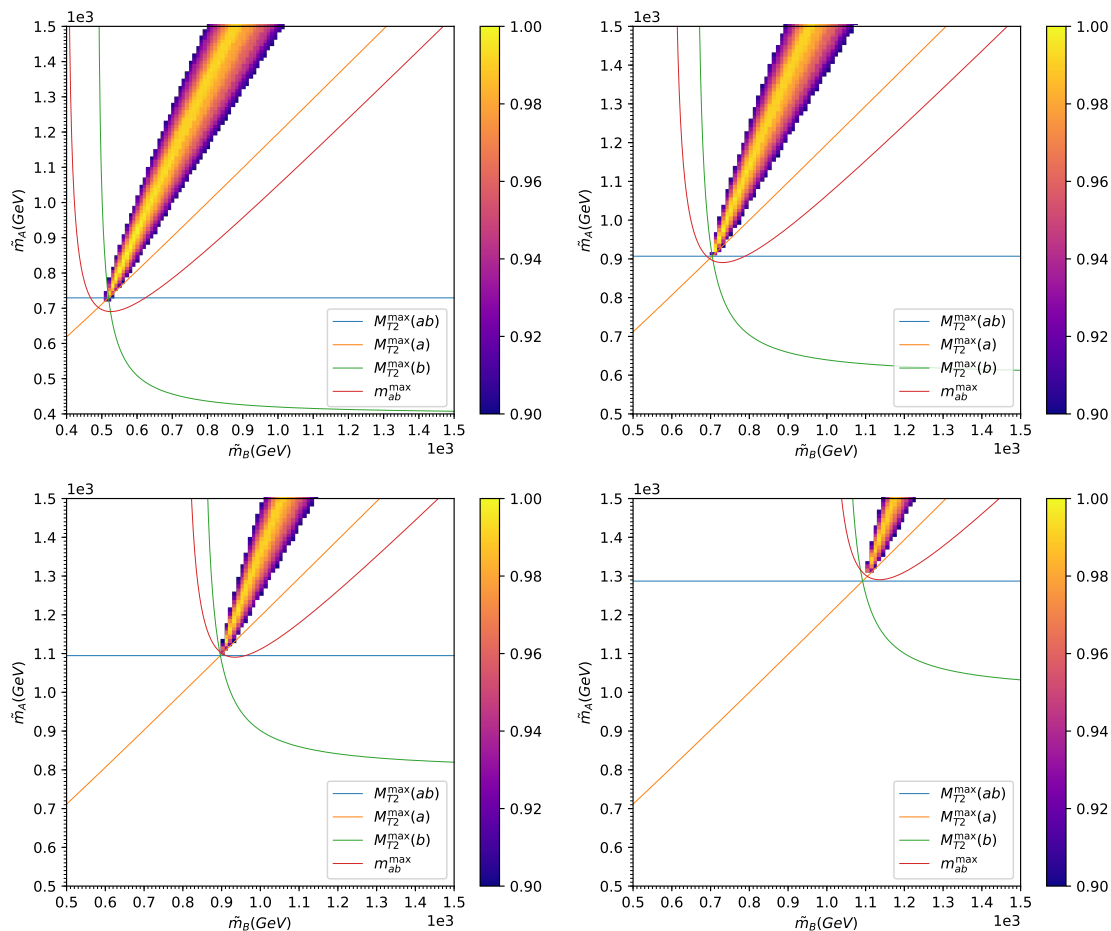
Figure 11. The same as figure 8, but for different values of $\tilde{m}_C$, not equal to the true mass $m_C = 700$ GeV. The top two plots have $\tilde{m}_C < m_C$: $\tilde{m}_C = 400$ GeV (top left) and $\tilde{m}_C = 600$ GeV (top right). The bottom two plots correspond to $\tilde{m}_C > m_C$: $\tilde{m}_C = 800$ GeV (bottom left) and $\tilde{m}_C = 1000$ GeV (bottom right). Note that for $\tilde{m}_C < m_C$ ($\tilde{m}_C > m_C$) it is the $m_{ab}^{\max}$ constraint (the $M_{T2}^{\max}(ab)$ constraint) which misses the region of high solvability.

as a function of $\tilde{m}_C$, we can identify the true m_C as the point where the maximum solvable fraction is highest. This is the technique proposed by H.-C. Cheng and Z. Han in ref. [66] (for an illuminating discussion on the relation between solvability and kinematic endpoints, edges and kinks, see [31, 71]).

In conclusion of this section, we have seen that the solvability method, supplemented with one or more kinematic endpoint measurements, is in principle capable of determining all three unknown masses m_A, m_B and m_C. However, as revealed by the preceding discussion in sections 4.2 and 4.3, the method is not as sensitive in finding the true value of m_C as it is in finding the true values of m_B and m_A, given m_C. This is indicative of a "flat direction" of low sensitivity along $\tilde{m}_C$. This is not unexpected — it is known that mass differences can be measured much better than the overall mass scale, as has been demonstrated with specific studies for the case of pair production [85–89] and a single decay chain [60, 61, 73, 90, 91].
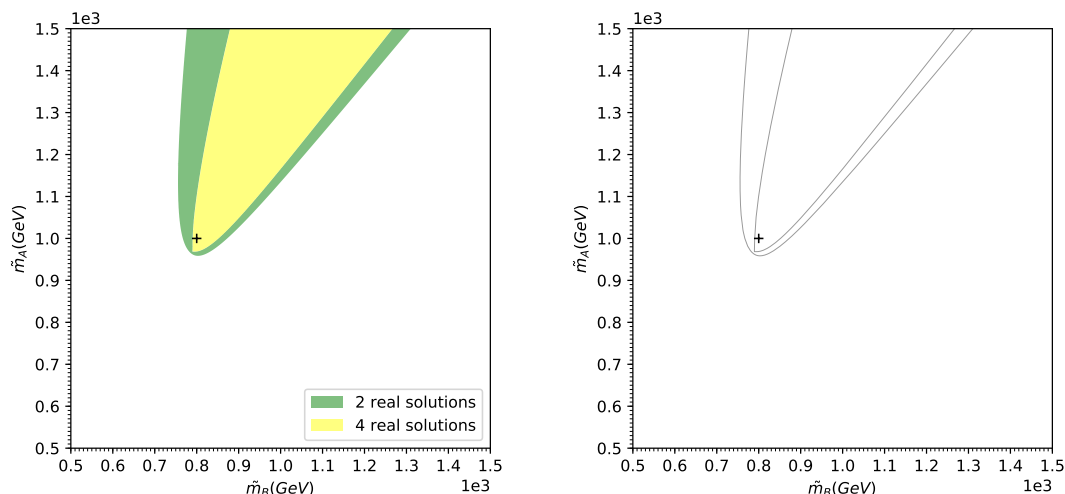
Figure 12. Illustration of degeneracy curves. We recycle the same event used to make the right panels in figures 2–4. On the left we show the solvability plot for $\tilde{m}_C = m_C = 700$ GeV, while on the right we show the corresponding degeneracy curves. As before, the cross marks the true mass point (m_B, m_A).

5 Extreme events and kinematic boundaries in mass space

With the intuition developed in the previous two sections, we are now ready to present our main idea. First we shall introduce some terminology.

5.1 Definitions

As illustrated in the solvability plots in figures 2–4, for any given event, the kinematic constraints (3.2) and (3.3) partition the three-dimensional parameter space $(\tilde{m}_A, \tilde{m}_B, \tilde{m}_C)$ into regions allowing 0, 2 or 4 real solutions for the invisible momenta. We shall call the two kinematic[10] boundary surfaces separating those mass space regions *degeneracy boundaries*, since *on* those boundaries there exists a pair of degenerate real solutions. For completeness, we shall also give a special name to the boundary separating the regions with zero and two solutions and call it a *solvability boundary*, since the event is solvable on one side of the boundary and not solvable on the other. In our event topology, the kinematic boundaries of an event are two dimensional *surfaces* in the three dimensional mass space $(\tilde{m}_A, \tilde{m}_B, \tilde{m}_C)$. Therefore, when we take a slice of the parameter space at fixed $\tilde{m}_C$ as in figures 2–4, we correspondingly obtain *degeneracy curves* in the $(\tilde{m}_B, \tilde{m}_A)$ plane, some of which (the ones which delineate the region with zero solutions) are *solvability curves*.

Figure 12 illustrates the notion of degeneracy curves, using the event from the right panels in figures 2–4. In the left panel of figure 12, we reproduce the solvability plot from figure 2 which was made for $\tilde{m}_C = m_C = 700$ GeV. Again we can see the three different regions — with 0, 2 and 4 real solutions (colored white, green and yellow, respectively). Then in the right panel of figure 12 we ignore the interiors of those regions and only plot the degeneracy curves for that event. As before, the cross marks the true mass point (m_B, m_A).

---

[10]In the sense that they are derived from kinematic constraints.

We observe that the cross does *not* lie on any of the degeneracy curves — indeed, there is no reason to think that the true masses will necessarily lead to degenerate real solutions for the momenta. Since the event used in figure 12 was chosen at random, its properties are generic and follow this expectation.

At the same time, figure 6 also revealed the presence of events in the sample for which the cross *will* lie on a degeneracy curve. Now is a good time to give a name to such special events, since they will be the main topic of discussion in this section. In general, whenever a given trial mass point $(\tilde{m}_A, \tilde{m}_B, \tilde{m}_C)$ lies on a degeneracy boundary of an event, the event will be said to be an *extreme* event *for that mass point*. Extreme events for the true mass point (m_A, m_B, m_C) will be referred to simply as extreme events. Note that *a priori* we do not know which events in the event sample are extreme in the latter sense, since we do not know the true masses. Therefore, in order to analyze extreme events, we either have to cheat and use Monte Carlo information, or develop some alternative strategies for recognizing such events in the data, see section 5.2 below.

As demonstrated in figure 6, the primary motivation for studying extreme events is that they are very efficient in ruling out incorrect mass hypotheses. This is especially important in the region *in the immediate vicinity of the true mass point*. Indeed, by definition, any event which is not extreme, will leave the whole neighborhood around the true mass point as viable. In that sense, extreme events are also *extremely* valuable, as they provide the only chance to probe the mass space close to the true mass point. This point is illustrated in figure 13, which repeats the exercise from figure 6 with three *other*, randomly selected, extreme events. Note that while the events were required to be extreme in the sense that the true mass point marked with the cross lies on a degeneracy boundary, they were *not* required to be complementary to each other, as was previously done in figure 6. As a result, their superposition now leaves a much larger red-shaded area in which all three events are solvable (compare to figure 6). Even so, notice that the true mass point is on the very tip of the allowed red-shaded region. In other words, three of the four possible directions away from the true mass point are ruled out, leaving only a relatively narrow funnel in the north-northeast direction. This is to be contrasted with the result from figure 5, for example, where the immediate vicinity of the true mass point is viable in any direction.

The observant reader would have noticed that each of the three events in figure 13 happened to be extreme because the true mass point lies on a solvability boundary as opposed to the other degeneracy boundary (the one between the regions with 2 and 4 real solutions). This is somewhat accidental — in the data sample we do find extreme events of both types. If we were to categorize them, we would find that the extreme events on a solvability boundary outnumber the others by a factor of roughly 5 : 1. This is consistent with the outcome in figure 13 — given three extreme events, the chances that they all have the true mass point on a solvability boundary are approximately $\left(\frac{5}{6}\right)^3 \approx 58\%$. One might question the usefulness of the remaining 1/6 of extreme events which do not involve a solvability boundary. Indeed, they do not help to *shave* the allowed mass space near the true mass point. Nevertheless, as we shall see in the next section, both types of extreme events will contribute on an equal footing to the mass measurement method proposed in section 6, therefore from now on we shall stop making the distinction between them.
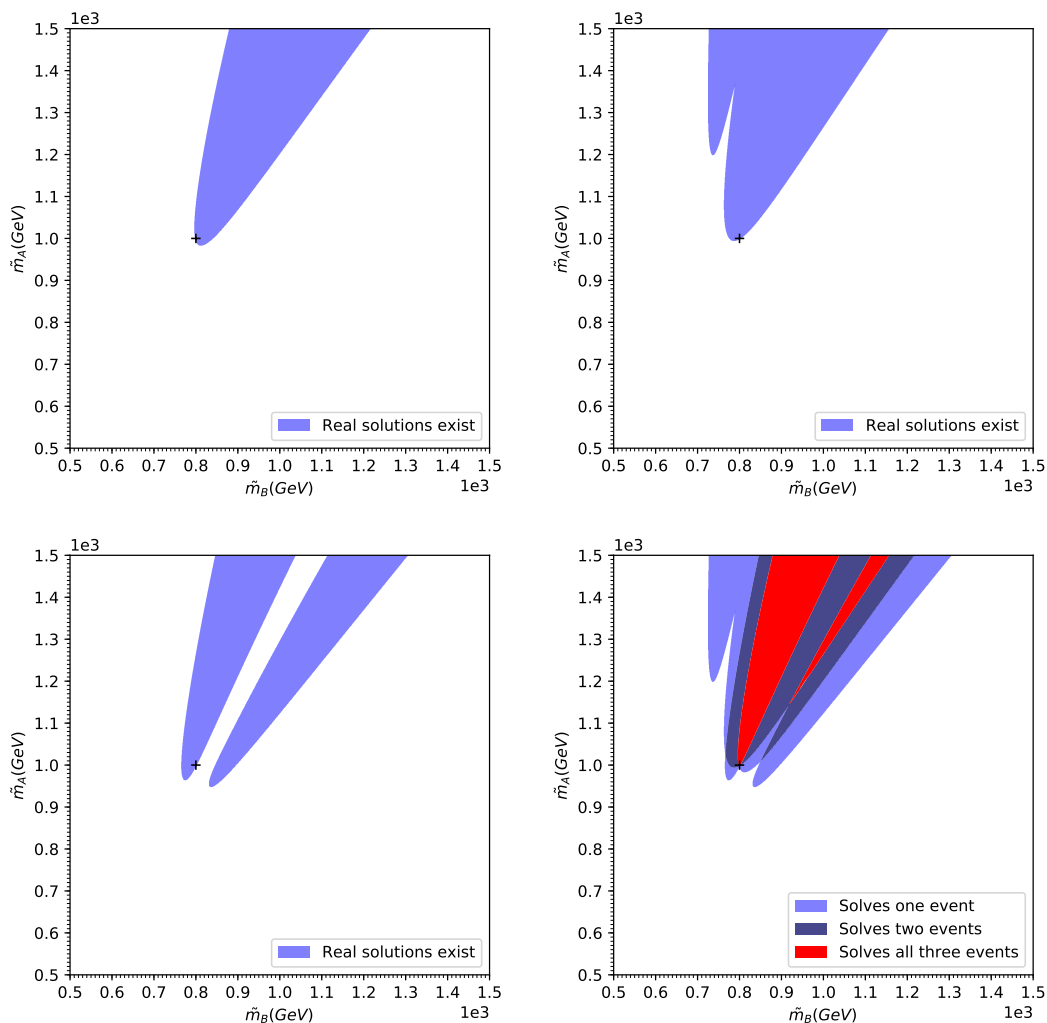
Figure 13. The same as figure 6, but for three other randomly chosen extreme events, i.e., the events were required to be extreme, but not necessarily complementary to each other.

5.2 Characterizing extreme events

As mentioned earlier, the kinematic constraints (3.2) and (3.3) allow four (in general complex) solutions for the invisible momenta q_i of particles C_i. The four solutions are continuous functions of $(\tilde{m}_A, \tilde{m}_B, \tilde{m}_C)$ and any non-real solutions among them appear in complex conjugate pairs [3]. On the degeneracy boundaries, where the number of real solutions changes, the equations have a pair of degenerate real solutions.

We can therefore characterize extreme events (for a given choice of masses $\tilde{m}_A$, $\tilde{m}_B$ and $\tilde{m}_C$) by finding the condition for a particular solution (q_1, q_2) to be degenerate. It can be shown that a solution (q_1, q_2) is degenerate iff

$$\mathcal{E}(p_{a_i}, p_{b_i}, q_i) \equiv E_{a_1} E_{b_1} E_{C_1} E_{a_2} E_{b_2} E_{C_2} \left[(\vec{V_1} \times \vec{V_2}) \cdot \hat{z} \right] = 0, \tag{5.1}$$

where $\hat{z}$ is the unit vector along the z-axis, the E's refer to the energy components of the

corresponding 4-momenta, and the three-vectors $\vec{V}_i$ are defined as

$$\vec{V}_i = (\vec{v}_{a_i} \times \vec{v}_{b_i}) + (\vec{v}_{b_i} \times \vec{v}_{C_i}) + (\vec{v}_{C_i} \times \vec{v}_{a_i}). \tag{5.2}$$

Here the 3-vectors $\vec{v}$ are the velocities[11] of the particles, i.e., $\vec{v} = \vec{p}/E$:

$$\vec{v}_{a_i} = \frac{\vec{p}_{a_i}}{E_{a_i}}; \quad \vec{v}_{b_i} = \frac{\vec{p}_{b_i}}{E_{b_i}}; \quad \vec{v}_{C_i} = \frac{\vec{q}_i}{E_{C_i}}. \tag{5.3}$$

Eq. (5.1) is useful in understanding the kinematic configurations of extreme events. As discussed later in section 5.4, extreme events correspond to kinematic endpoints, therefore eq. (5.1) (and its analogues for other topologies) can be useful in understanding and deriving various endpoints. Eq. (5.1) also provides an efficient way of generating a pure sample of extreme events for dedicated studies of such events.[12] Of course, the quantity $\mathcal{E}$, being a scalar, conveniently quantifies the level of extremeness of the event: the smaller the magnitude of $\mathcal{E}$, the more extreme an event is.

One downside of the parametrization (5.1) is that it refers to the particular solution (q_1, q_2), so that in order to use this criterion in practice, one has to solve the constraint equations first. Since they may lead to up to 4 real solutions, one must test the condition (5.1) for each real solution and then use the smallest value of $\mathcal{E}$ thus obtained in order to judge whether the event is extreme or not.

5.3 Extreme events are more common than you think

Having motivated extreme events through their useful and interesting properties, the crucial question to address next is, how frequent are they in a realistic data sample? The pessimist from section 4.1 could again raise an objection that the volume of a two-dimensional surface in three-dimensional space is zero, and therefore, the chances that an event will land exactly on a degeneracy boundary and thus become extreme are vanishing as well. However, this argument contains a hidden assumption — that the distribution of events throughout the three-dimensional space is a normal, well-behaved function, i.e., the event density has no singularities. In this subsection we shall argue that the hidden assumption is false, and that in fact, in the narrow width approximation, the density of events is expected to be singular *precisely* on the degeneracy boundaries, thus greatly increasing the odds of encountering extreme events in the sample. The gist of our argument goes back to the algebraic singularity method of I.-W. Kim [68]. As a specific example, phase space singularities on kinematic surfaces were recently explored in the case of a single SUSY-like decay chain in [72, 73, 75]. However, our main argument here is very general, thus we shall try to keep the discussion independent of the underlying topology.

Consider the space of the $N_{p \cup q}$ components of the 4-momenta of all final state particles, visible and invisible. Out of these, let N_p be the total number of visible momentum components $\{p\}$ and N_q be the total number of invisible momentum components $\{q\}$,

---

[11]Not to be confused with the spatial components of the 4-velocities.

[12]Any simulated event (for which we know the invisible momenta) can be converted into an extreme event by appropriately rotating the decay of B_2 about its direction of motion to satisfy eq. (5.1).

where trivially $N_{p \cup q} = N_p + N_q$. On-shell events generated from a given set of true masses will obey a certain number, C_q, of kinematic constraints involving the invisible momenta, plus possibly also a certain number of constraints C_p involving *only the visible* momenta $\{p\}$ and no unknown parameters. As a result of the kinematic constraints, the final state momenta will lie on a hypersurface of dimension $N_{p \cup q} - C_q - C_p$, which is embedded in the original ($N_{p \cup q}$)-dimensional space. This hypersurface represents the full phase space for this process, and events will be more or less evenly distributed in the full phase space.

Now the crucial question is, how are events distributed in the allowed ($N_p - C_p$)-dimensional *visible* subspace? For this purpose, we need to project the full ($N_{p \cup q} - C_q - C_p$)-dimensional phase space onto the ($N_p - C_p$)-dimensional allowed visible subspace [68]. The dimensionality of the resulting projection is

$$\min\left(N_{p \cup q} - C_q - C_p, N_p - C_p\right). \tag{5.4}$$

In this paper, we shall restrict our attention to the case where $N_{p \cup q} - C_q - C_p = N_p - C_p$, i.e., the dimensionality of the full phase space equals the dimensionality of the allowed visible subspace. Since $N_{p \cup q} = N_p + N_q$, an equivalent way to state the same condition is simply $N_q = C_q$, i.e., there are just enough constraints in order to solve for the invisible momenta $\{q\}$. This was precisely the case in section 3: we were able to solve for the invisible momenta in the event topology of figure 1. Let us check: there were 4 visible final state particles ($N_p = 4 \times 4 = 16$), 2 invisible final state particles ($N_q = 2 \times 4 = 8$), two constraints from (3.2) and six constraints from (3.3) for a total of $C_q = 2 + 6 = 8$. There are also four mass shell constraints on the visible momenta ($C_p = 4$). Thus both the full phase space and the visible phase space are 12-dimensional: $N_{p \cup q} - C_q - C_p = (16 + 8) - 8 - 4 = 12$ and $N_p - C_p = 16 - 4 = 12$.

As already mentioned above, the probability density of events on the full phase space is well behaved, i.e., there are no singularities or discontinuities. However, this is not the case with events in the visible phase space. First we note that the mapping of the full phase space onto the visible phase space is not one-to-one (or invertible) — multiple points in the full phase space can have the same visible phase space projection, as evidenced by the existence of multiple solutions for the invisible momenta. To keep a simple visual analogy in mind, think of the projection of a two-dimensional hollow sphere onto the equatorial plane. Any image point in the equatorial plane has two possible preimages, one in the Northern hemisphere and one in the Southern hemisphere.

Let $\mathcal{P}_{\text{full}}$ be the density of events in the full phase space, and let $\mathcal{P}_{\text{vis}}$ be the density of events in the visible phase space. Consider an infinitesimal volume dV_{vis} in the visible phase space and the corresponding infinitesimal volumes $dV_{\text{full},i}$ which can be mapped onto it from the full phase space. Here the index i labels the "sheet" on which $dV_{\text{full},i}$ is located[13] — for example, in the hollow sphere example above, the two values of $i = 1, 2$ would label the Northern and Southern hemispheres. The two event densities are related as

$$\mathcal{P}_{\text{vis}} \, dV_{\text{vis}} = \sum_i \mathcal{P}_{\text{full},i} \, dV_{\text{full},i}, \tag{5.5}$$

---

[13]Since the visible phase space and the full phase space have equal dimensionalities, there can only be a finite number of such "sheets".

or equivalently,

$$\mathcal{P}_{\text{vis}} = \sum_i \mathcal{P}_{\text{full},i} \, \frac{dV_{\text{full},i}}{dV_{\text{vis}}}. \tag{5.6}$$

As already mentioned, $\mathcal{P}_{\text{full},i}$ is well behaved. However, at points where $dV_{\text{vis}}/dV_{\text{full},i}$ is vanishing (for one of the i values), $\mathcal{P}_{\text{vis}}$ will be singular [68]. The vanishing of $dV_{\text{vis}}/dV_{\text{full},i}$ occurs at those locations where the tangent plane of the full phase space is perpendicular to the tangent plane of the visible phase space. (In the hollow sphere example above, this singularity occurs on the equator, where the surface of the sphere is perpendicular to the equatorial plane.) It is also easy to see that those locations are precisely where two different branches in the full phase space (i.e., corresponding to two different values of i) meet (in the hollow sphere example, think of the Northern and Southern hemisphere merging at the equator). In other words, the points where $\mathcal{P}_{\text{vis}}$ is singular correspond to extreme events which have degenerate real solutions for the invisible momenta. Consequently, the dimensionality of the subspace spanned by extreme events is $N_p - C_p - 1$, due to the additional "degeneracy condition".

5.4 The connection between extreme events and kinematic endpoints

For events on the boundary of the visible phase space, the true mass point will lie on the solvability boundary in mass space. In other words, events on the boundary of the visible phase space lead to a particular class of extreme events, namely the ones involving the solvability boundary. As already discussed at the end of section 5.1, those are the large majority of extreme events.

The shape of the boundary of the visible phase space is dependent on the underlying mass spectrum and can therefore reveal information about it. A standard approach to extract this information is to measure kinematic endpoints in the distributions of variables suitably constructed from the visible momenta [14, 63]. It is clear that the events for which the kinematic variable under consideration acquires its endpoint value, are necessarily events on the boundary of the visible phase space [31, 66, 71]. Since those are extreme events, it follows that extreme events are responsible for the endpoints in the distributions of kinematic variables. The reverse, however, is not necessarily true — not *all* of the extreme events are necessarily mapped onto the kinematic endpoint value. Therefore, compared to endpoints in kinematic distributions, extreme events present an interesting and more general target for studies of event kinematics.

5.5 The distribution pattern of kinematic boundaries in mass space

In section 5.3 we argued that the density of extreme events is singular. Here we shall use that result to show that if we consider the degeneracy boundaries in the mass space for a sample of events, the density of these boundaries will be singular at the true mass point.

We shall first give a heuristic justification before building it into a more rigorous argument. Note that any event is extreme for some set of points in mass space, namely, the ones on the degeneracy boundaries of that event. We do not know *a priori* whether any of those mass points happen to be the true masses or not. So let us then try to

figure this out on a statistical basis. Let each event give a vote to all the mass points on its degeneracy boundaries, i.e., all masses for which it is extreme. We saw in section 5.3 that events which are extreme for the true mass have an enhanced (singular) probability density. On the other hand, events which are extreme for an incorrect test mass point do not necessarily have the same enhancement. By this logic, we can expect the true mass point to pick up more votes in this procedure than an incorrect test mass choice. "More votes" here corresponds to a higher density of degeneracy boundaries.

Let us rephrase this heuristic argument in a slightly more rigorous form. We shall do this by mapping the density of extreme events in the visible phase space to the density of degeneracy boundaries in the mass space.

In our event topology of figure 1 the mass space is 3 dimensional and the degeneracy boundaries are 2 dimensional surfaces. Their density, $\mathcal{P}_{\text{mass}}^{db}(\tilde{m}_A, \tilde{m}_B, \tilde{m}_C)$, will be defined as the fraction of degeneracy boundaries per unit $\sqrt[3]{\text{volume}}$ in the mass space.[14] It is given by

$$\mathcal{P}_{\text{mass}}^{db}(\tilde{m}_A, \tilde{m}_B, \tilde{m}_C) \sqrt[3]{d^3 V_{\text{mass}}} = dV_1 \int\limits_{\substack{\text{extreme} \\ \text{events}}} \mathcal{P}_{\text{vis}} \, dV_{(N_p - C_p - 1)}, \tag{5.7}$$

where the integral is over the $(N_p - C_p - 1)$-dimensional subspace of extreme events for the given mass point $(\tilde{m}_A, \tilde{m}_B, \tilde{m}_C)$. dV_1 represents a differential element in the visible phase space perpendicular to the space of extreme events. It corresponds to the change in the space of extreme events when the mass point varies within $d^3 V_{\text{mass}}$. It helps to think of the space of extreme events of a test mass as an $(N_p - C_p - 1)$-dimensional curve which changes smoothly when the test mass changes. Eq. (5.7) can be rewritten as

$$\mathcal{P}_{\text{mass}}^{db}(\tilde{m}_A, \tilde{m}_B, \tilde{m}_C) = J \int\limits_{\substack{\text{extreme} \\ \text{events}}} \mathcal{P}_{\text{vis}} \, dV_{(N_p - C_p - 1)}, \tag{5.8}$$

where J is a Jacobian factor. We can see that $\mathcal{P}_{\text{mass}}^{db}$ will be singular iff the integral is divergent.

Note that the Jacobian factor and the integration volume for a given test mass are both independent of the true mass from which the event sample is generated. So, except possibly for some special test masses (special overall, not in relation to the true mass), we can expect their contribution to the variation of $\mathcal{P}_{\text{mass}}^{db}$ to be well-behaved. Any local singularity in $\mathcal{P}_{\text{mass}}^{db}$ can therefore only come from $\mathcal{P}_{\text{vis}}$. As mentioned in section 5.3, $\mathcal{P}_{\text{vis}}$ is singular for extreme events of the true mass and for those events only. Thus the density of degeneracy boundaries in the mass space is singular at the true mass.[15]

---

[14]This is because the number of randomly distributed d-dimensional objects in a D-dimensional volume element scales as $(\text{volume})^{(1-d/D)}$. In our case $d = 2$ dimensional surfaces are distributed in a $D = 3$ dimensional volume element and their number scales as $(\text{volume})^{1/3}$.

[15]The density is also singular at masses whose extreme events have an intersection of measure greater than 0 with the true extreme events.

6 The kinematic focus point method

6.1 The basic idea

Before proceeding further, let us condense the content of section 5.5 into the following elevator pitch:

1. Draw the degeneracy boundaries (in the mass space) for all events in the data sample. As a reminder, the degeneracy boundary of an event contains masses for which the given event has degenerate real solutions for the invisible momenta.

2. The density of these boundaries should peak at the true mass point.

This lays out a straightforward mass determination method pictorially illustrated in figures 14 and 15. We simply plot the degeneracy surfaces for *all* events in our sample, and look for a focus point where a maximal number of them either intersect or pass close by. Since it is difficult to visualize this in the full three dimensional mass space $(\tilde{m}_A, \tilde{m}_B, \tilde{m}_C)$, in figures 14 and 15 we show results in the $(\tilde{m}_A, \tilde{m}_B)$ plane for fixed $\tilde{m}_C = m_C = 700$ GeV. In figure 14 we use the same plot range as in all of our previous figures, and gradually increase the number of events used for the plot from 5 (top left panel) to 50 (bottom right panel). We observe that as we add more and more events, a focus point indeed gradually emerges near the true mass values of $m_B = 800$ GeV and $m_A = 1000$ GeV. Our method derives it name from this feature, since the degeneracy curves tend to "focus" at the true mass point. The focus point is very easy to identify by eye, and in the next subsection we shall develop a procedure for quantifying the observed amount of "focusing". Clearly, if we add even more events, the focus point should become even more pronounced, but unfortunately, the plot would become too cluttered. This is why when we further increase the number of events to 100 in figure 15, we zoom in on the region in the vicinity of the focus point. The left (right) panel of figure 15 uses a zoom factor of 5 (10) relative to the plot range in figure 14. We see that the focus point is very clear, and is in perfect agreement with the true values $m_B = 800$ GeV and $m_A = 1000$ GeV. For example, if one were to estimate the values of m_B and m_A by simply eyeballing the plots in figure 15, the error would not be more than a couple of GeV! One should also keep in mind that the plots in figure 15, which were made only for illustration, use only 100 events, while the actual LHC statistics is likely to be much higher.

6.2 Measuring m_B and m_A for a given trial mass $\tilde{m}_C$

Hopefully by now the reader has been convinced by the money plots in figures 14 and 15 that the kinematic focus point method outlined in the previous section 6.1 is a promising new technique for mass measurements. In the remainder of this section, we shall discuss how to implement it in practice, as well as some practical challenges and how they might impact the sensitivity of the method.

Since the kinematic focus point method relies on the high density of degeneracy curves near the true mass point, we need to design a procedure for quantifying this effect. Following the outline of section 4, let us first concentrate on the task of measuring m_B and m_A at
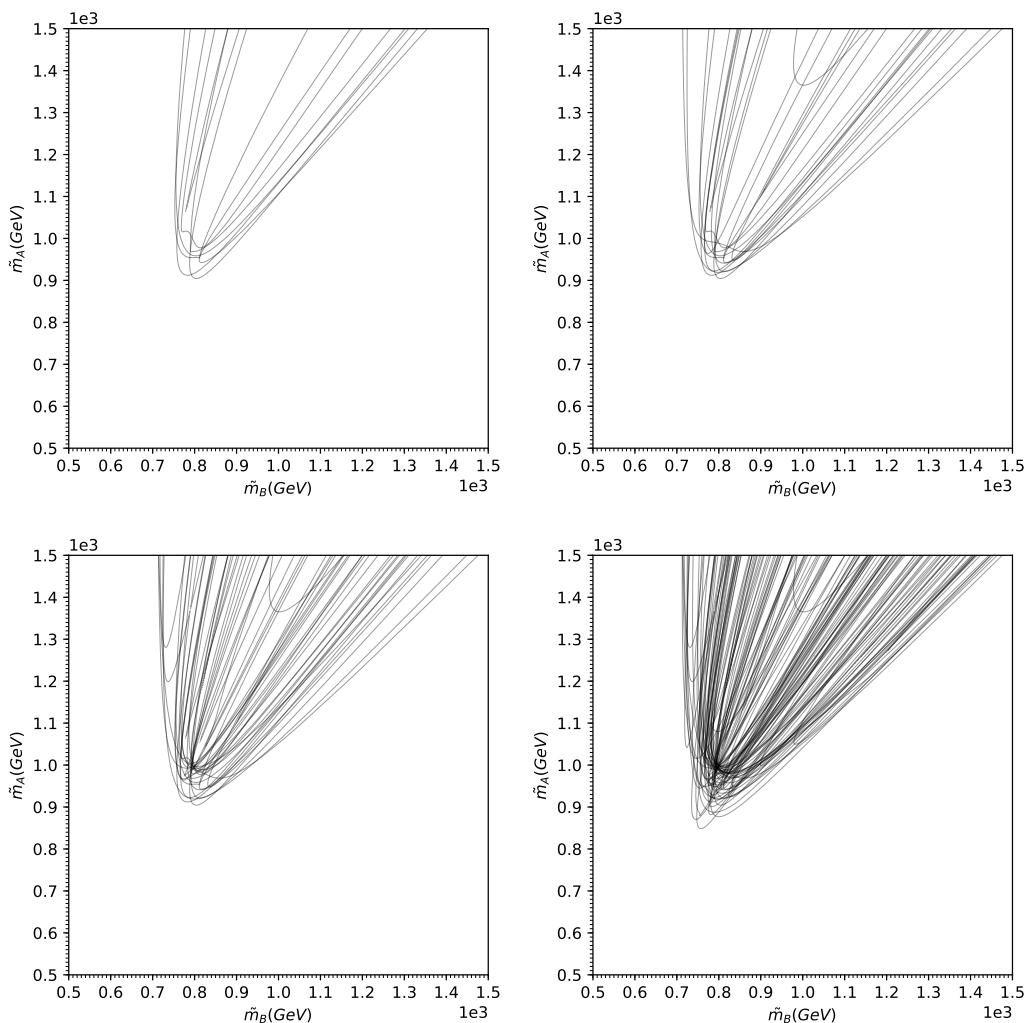
Figure 14. Degeneracy curves in the $(\tilde{m}_B, \tilde{m}_A)$ plane, for fixed $\tilde{m}_C = m_C = 700$ GeV. The plots are made with an increasing number of events: 5 events (top left), 10 events (top right), 20 events (bottom-left) and 50 events (bottom right). Each subsequent panel already contains the events plotted previously, plus some new events. Note the gradual emergence of the focus point of boundary curves near the true mass $m_B = 800$ GeV and $m_A = 1000$ GeV.

a fixed value of $\tilde{m}_C$, postponing the task of measuring m_C until the next section 6.3. For this purpose, we need to plot one-dimensional degeneracy curves in the two-dimensional $(\tilde{m}_B, \tilde{m}_A)$ plane, as was done in figures 14 and 15. The discussion from section 5.5 showed that the relevant quantity in that case is the number of degeneracy curves per unit $\sqrt{\text{area}}$, which is what we shall use in our analysis. The area elements in the $(\tilde{m}_B, \tilde{m}_A)$ plane will be chosen to be 10 GeV × 10 GeV squares, and so the resulting unit for the density of degeneracy curves will be $(10 \text{ GeV})^{-1}$. For the remainder of this subsection, the test mass $\tilde{m}_C$ will be set to the true value of 700 GeV.

We are now ready to study the density of degeneracy curves in the $(\tilde{m}_B, \tilde{m}_A)$ plane. The result is shown as a heat map in figure 16 and as 3D histograms from different viewpoints
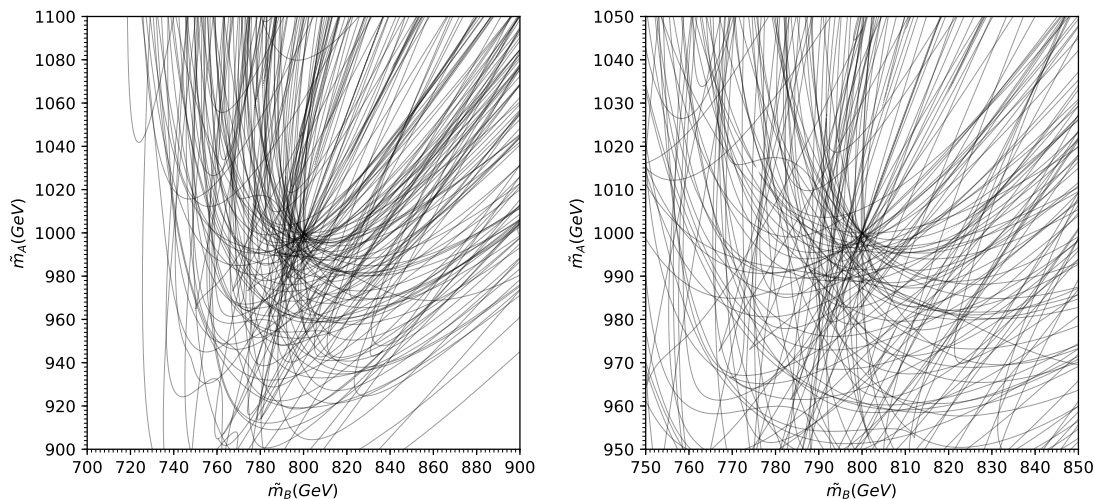
Figure 15. The same as figure 14, but with 100 events and zoomed in by a factor of 5 (left panel) and a factor of 10 (right panel).
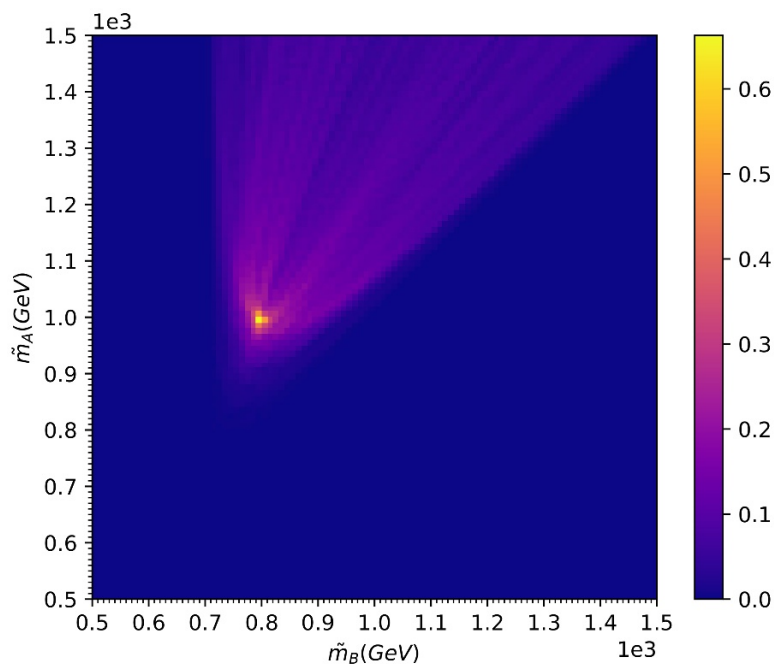

Figure 16. A heat map of the density of degeneracy curves in the $(\tilde{m}_B, \tilde{m}_A)$ plane for $\tilde{m}_C = m_C = 700$ GeV. The density is displayed in units of fraction of events per 10 GeV. Note the sharp peak at the true values $m_B = 800$ GeV, $m_A = 1000$ GeV — over 60% of the signal events have a degeneracy curve passing through a 10 GeV × 10 GeV square around the true mass point.

in figure 17. The density of degeneracy curves is displayed in units of fraction of events per 10 GeV, i.e., instead of plotting the total number of curves passing through a given 10 GeV × 10 GeV square, we plot the fraction of events in the sample which have a degeneracy curve passing through that square. By normalizing to a fraction, our results become insensitive to the statistics used to make the plots (in this case, figures 16 and 17
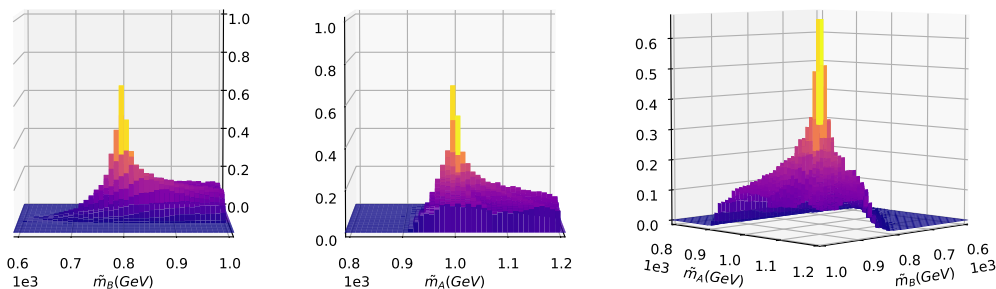
Figure 17. The same as figure 16, except densities are plotted as a 3D histogram instead of a heatmap. The three figures show the 3D histogram from different angles. The peak is at the true mass $m_B = 800$ GeV, $m_A = 1000$ GeV.

were made with 1000 events). The figures show that the density has a sharp peak at the true mass ($m_B = 800$ GeV, $m_A = 1000$ GeV). The peak is actually very well pronounced: note that over 60% of the events in the sample have one of their degeneracy curves passing through a 10 GeV × 10 GeV square around the true mass point. This confirms that our method is really effective in finding m_B and m_A, given $\tilde{m}_C$. Note the advantages of our method over the solvability method from section 4 — first, we do not encounter the flat direction of 100% solvability seen in figures 7, 9 and 10, and as a result we do not need any additional experimental information (from kinematic endpoints or otherwise); and second, we are measuring a sharp peak structure which is centered on the true values of the particle masses.

6.3 Measuring m_C

As in section 4.3, we now turn to the more difficult task of measuring m_C. For this purpose, we repeat the exercise from the previous subsection, only this time with different values of $\tilde{m}_C$. Heat maps analogous to the one in figure 16 are shown in the left and right panel of figure 18 for two representative values, $\tilde{m}_C = 400$ GeV and $\tilde{m}_C = 1000$ GeV, respectively. We observe that each of the two plots in figure 18 exhibits its own density peak in the $(\tilde{m}_B, \tilde{m}_A)$ plane. As expected, the location of the peak tracks the value of $\tilde{m}_C$ — for lower (higher) values of $\tilde{m}_C$, the peak is located at lower (higher) values of $\tilde{m}_B$ and $\tilde{m}_A$. From that point of view, there is no qualitative difference in the heat maps at different values of $\tilde{m}_C$. However, there is a quantitative difference: the height of this peak, i.e, the maximum density in the $(\tilde{m}_B, \tilde{m}_A)$ plane for a given value of $\tilde{m}_C$, is different for different values of $\tilde{m}_C$. The maximum height is expected to occur at the true value of $\tilde{m}_C = m_C$. While this expectation is consistent with the results in figures 16 and 18, we quantify it further in figure 19, which shows a plot of the maximum density of degeneracy curves in the $(\tilde{m}_B, \tilde{m}_A)$ plane (after fixing the value of $\tilde{m}_C$), as a function of $\tilde{m}_C$. As before, the density is plotted in units of fraction/(10 GeV). Figure 19 nicely confirms that the density peaks at the true value of $m_C = 700$ GeV (marked with the vertical red line). As already discussed in section 4.3, the m_C measurement is rather challenging — in our case this is evidenced by the fact that the peak in figure 19 is not as sharp as the peak in figures 16 and 18. Nevertheless, figure 19 confirms that in principle our method can be used to find m_C as well.
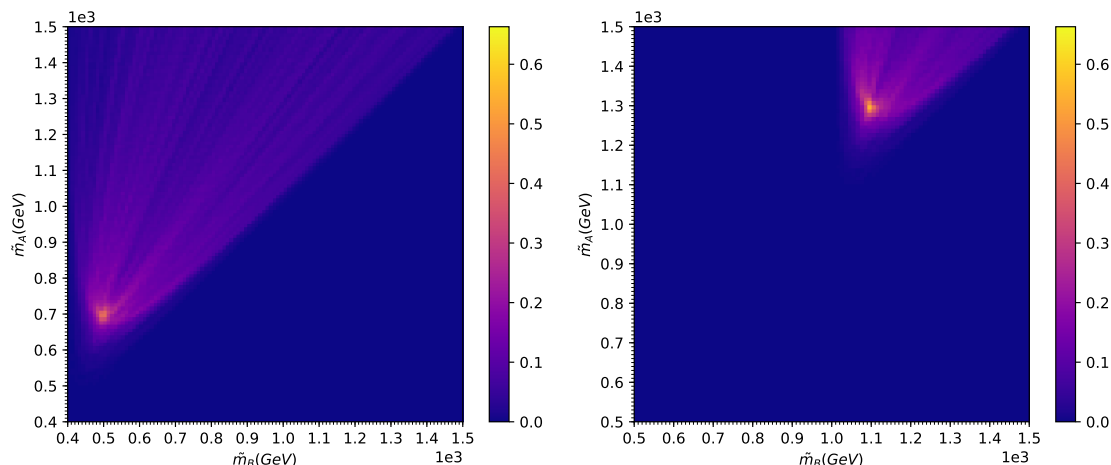
– 29 –

Figure 18. The same as figure 16, but for $\tilde{m}_C = 400$ GeV (left panel) and $\tilde{m}_C = 1000$ GeV (right panel).
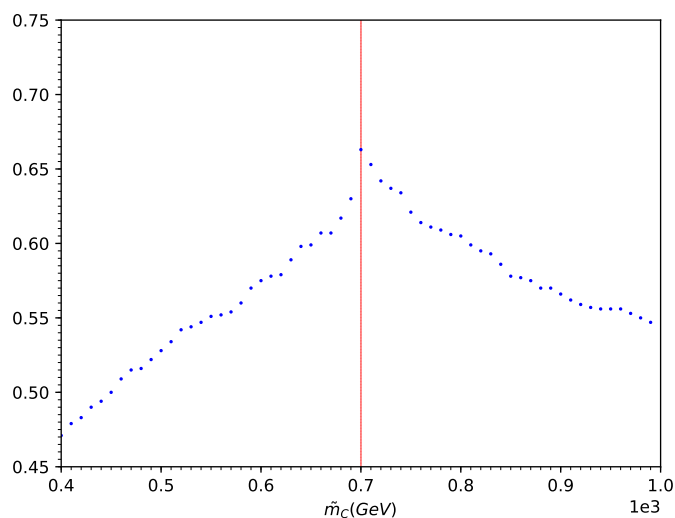

Figure 19. Plot of the maximum density of degeneracy curves (in units of fraction/(10 GeV)) for different fixed values of $\tilde{m}_C$. For each value of $\tilde{m}_C$, the maximization is done in the $(\tilde{m}_B, \tilde{m}_A)$ plane. The peak value in the plot is observed at the true value of $m_C = 700$ GeV marked with the vertical red line.

6.4 The impact of the detector resolution

Until now, all of our studies were done at the parton level and in the narrow width approximation, without smearing from either detector resolution or particle width effects. We shall now investigate the size of those effects. In this subsection we shall first add the effect of the detector resolution. We shall consider the typical scenario where the particles a_i and b_i in the event topology of figure 1 are bottom quarks and leptons, respectively. Correspondingly, we shall apply smearing to the energies of the two b-jets according to typical LHC resolutions [92]: for jet p_T up to $\{10, 20, 30, 50, 100, 400, 1000\}$ GeV, the p_T-dependent energy resolution parameter is $40\%, 28\%, 19\%, 13\%, 10\%, 6\%, 5\%$.
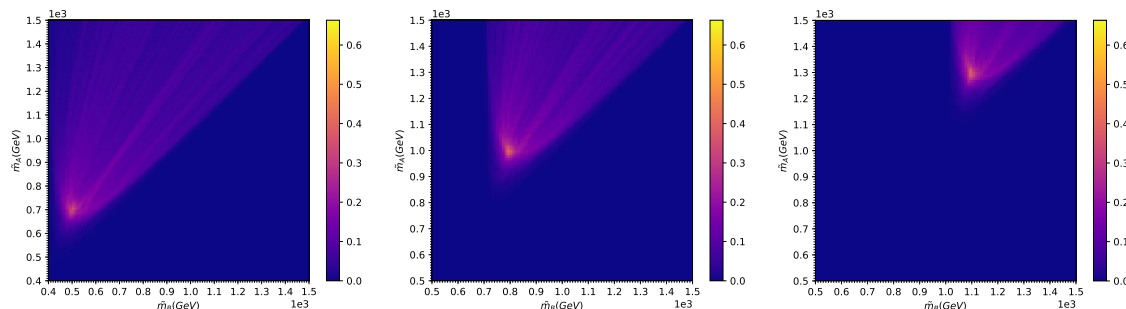
Figure 20. The same as figures 16 and 18, but including the effects of jet smearing. The left (middle, right) panel shows results for fixed $\tilde{m}_C = 400$ GeV ($\tilde{m}_C = 700$ GeV, $\tilde{m}_C = 1000$ GeV).
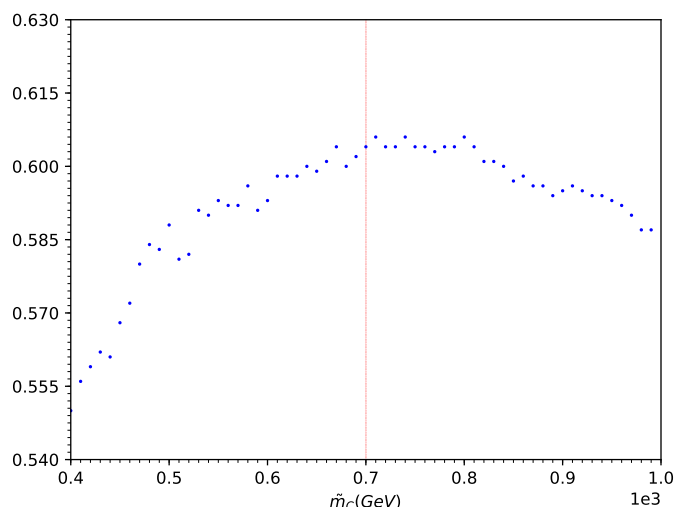

Figure 21. The same as figure 19, but including the effects of jet smearing and counting events in a larger (30×30 GeV) collection bin.

Figures 20 and 21 show the results analogous to figures 16, 18 and 19, only now with the detector resolution included. As expected, the detector effects tend to wash out the peak structures a little bit. Nevertheless, the peaks in figure 20 (which shows measurements of m_A and m_B for fixed $\tilde{m}_C$) are still pronounced, and more importantly, the peak found for $\tilde{m}_C = m_C$ is still located at the proper values of the masses. Figure 21 shows the measurement of m_C (in the presence of detector effects), which was already a difficult task even at the gen-level, see figure 19.

6.5 A standard model example: dilepton $t\bar{t}$ events

Most of the mass measurement methods applicable to LHC events with missing transverse energy were developed with some kind of new physics model in mind, e.g., supersymmetry [63]. However, experimenters who wish to test the kinematic focus point method in real data do *not* have to wait for the discovery of any new physics — the event topology of figure 1 is already present in the LHC data in the form of Standard Model dilepton $t\bar{t}$ events, for which the available statistics is enormous. Therefore, it is worth supplementing
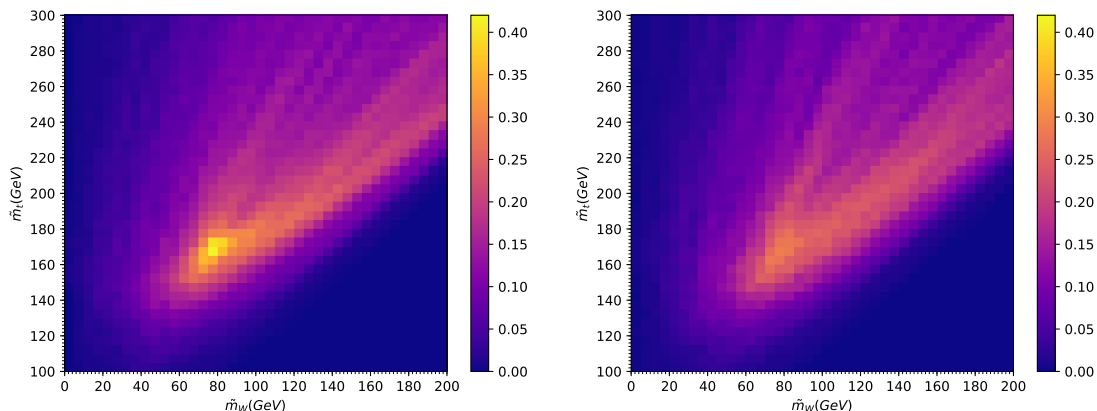
Figure 22. Density of degeneracy curves for Standard Model dilepton $t\bar{t}$ events in the $(\tilde{m}_W, \tilde{m}_t)$ plane for $\tilde{m}_\nu = m_\nu = 0\,\mathrm{GeV}$, without detector smearing (left) and with detector smearing (right). Unlike figures 16, 18 and 20, the density units here are fraction of events per 5 GeV, i.e., the bins are 5 GeV × 5 GeV.

our previous results with a study showcasing the method for the dilepton $t\bar{t}$ channel, and this is what we shall do in the current subsection.

We generate Standard Model $t\bar{t}$ events with MADGRAPH [81], using the proper widths for the top quark and the W boson. We select dilepton events in which both top quarks have decayed leptonically, and repeat the kinematic focus point analysis from section 6.2, setting the trial neutrino mass $\tilde{m}_\nu$ to zero. We then consider the plane spanned by the trial masses for the W boson ($\tilde{m}_W$) and for the top quark ($\tilde{m}_t$) and compute the density of the degeneracy curves. The heat map analogous to figure 16 is shown in figure 22, where the left panel depicts the parton level result, while in the right panel we include the effects from the detector smearing as in section 6.4.

As anticipated, figure 22 reveals a peak structure near the true masses $m_W = 80$ GeV and $m_t = 173$ GeV. The peak is especially pronounced at the parton level (left panel) — over 40% of the events have a degeneracy curve passing through a 5 GeV × 5 GeV square nearby. The detector resolution does tend to wash out the peak structure in the right panel, but a maximum is still visible. This suggests that the kinematic focus point method could allow the simultaneous independent measurement of the top and W-boson masses in the spirit of refs. [13, 30].

7   Conclusions and outlook

In this paper we propose a new approach to mass measurements in events with missing energy, called the kinematic focus points method. The method derives from the study of the solvability of the kinematic constraints which are present in a given event topology [15–20, 31, 66]. Using the dilepton $t\bar{t}$ topology as our example, we first critically examined the solvability method for measuring masses, and its relation to the measurements of kinematic endpoints. We then showed that any given event divides the relevant three-dimensional mass parameter space into regions with a certain number of (pairs of) real solutions for the
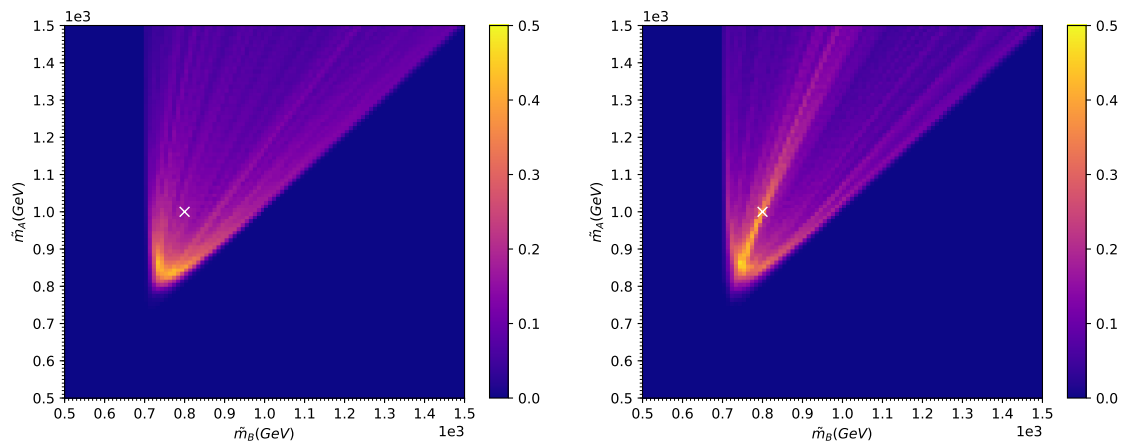
Figure 23. The same as figure 16, for Standard Model dilepton $t\bar{t}$ background events (left panel) and preselected signal events (right panel), both for $\tilde{m}_C = 700\,\text{GeV}$. The signal events entering the plot on the right have been preselected to obey all four kinematic endpoints (4.1) predicted for the Standard Model dilepton $t\bar{t}$ background. The white $\times$ symbol marks the location (m_B, m_A) of the true masses in the signal topology.

unknown invisible momenta. The surface boundaries between those regions are where the solutions become degenerate, and we called those surfaces "degeneracy boundaries". We illustrated and studied the shape of the degeneracy boundaries, as well as their distribution throughout the mass parameter space. In particular, we singled out a special class of events, extreme events, for which the true mass point lies on a degeneracy boundary.

Our main results were:

- Extreme events are very efficient in restricting the allowed mass parameter space.

- Extreme events are abundant in realistic data samples, due to singularities in the phase space distribution.

- This abundance of extreme events can be harnessed by drawing the degeneracy boundaries in the mass parameter space over the full event sample. The boundaries tend to focus at the true mass point and this property can be used to identify the true masses.

- our study of the solvability mass measurement method revealed a flat direction of nearly 100% solvability, which can be lifted only by adding additional information.

The kinematic focus points method has similarities to traditional mass-bump methods, thus allowing for data driven estimation of the relevant backgrounds.

The method also represents an improvement over the traditional kinematic endpoint techniques. The main advantage stems from the fact that we are able to extract useful information from *all* events and not just those which populate the vicinity of a kinematic endpoint. In order to illustrate this idea, we can look at the performance of the focus point method on a subset of events which would not assist in the standard extraction of the

kinematic endpoints of the signal through a fit. The mass spectrum for our study point ($m_A = 1000$ GeV, $m_B = 800$ GeV and $m_C = 700$ GeV) happens to be such that all four kinematic endpoints (4.1) for the signal are higher than the respective endpoints for the $t\bar{t}$ background. Therefore, by restricting ourselves to signal events which satisfy all four *background* endpoints, we can select signal events far away from the signal endpoints; such events are also hard to distinguish kinematically from the background.

In figure 23 we contrast the heat maps (created as in figure 16) for Standard Model dilepton $t\bar{t}$ background events (left panel) and so preselected signal events (right panel), both for $\tilde{m}_C = 700$ GeV. The white $\times$ symbol marks the location (m_B, m_A) of the true masses in the signal topology. The signal events entering the plot on the right have been preselected to obey all four kinematic endpoints (4.1) predicted for the Standard Model dilepton $t\bar{t}$ background. Therefore, as far as kinematic endpoints are concerned, these signal events are very hard to distinguish from the SM background, and in particular, cannot be used for discovery [51]. Yet the heat map for these "low utility" signal events in the plot on the right still shows a distinct feature through the correct masses, which is not present for the SM case shown in the left panel.[16]

The focus point method is based purely on event kinematics, and is therefore quite model-independent. Note that in addition to measuring the masses of particles, this technique can also be used as a new physics search technique by designing an analysis which would look for a bump feature in the density of the kinematic boundaries.

Acknowledgments

A The flat direction of low sensitivity in mass space

The numerical results in sections 4.3 and 6.3 suggested the presence of a region ("flat direction") in mass space which has relatively low sensitivity. In other words, the analysis is least sensitive to the degree of freedom (in mass parameter space) parametrizing the flat direction. In this appendix we identify and parametrize the flat direction.

One of the key ideas in deriving the flat direction is that the kinematic constraints (3.2) and (3.3) are a) Lorentz invariant and b) invariant under separate longitudinal boosts of the two branches in figure 1. Therefore, without loss of generality we can restrict our attention to events in which both A_1 and A_2 are produced at rest in the longitudinal direction, and have equal and opposite transverse momenta. The other key idea is that the flat direction

---

[16]The absolute maximum in the right plot of figure 23 is shifted away from the white $\times$ symbol due to the bias introduced by the applied preselection. Once the whole signal sample is considered, the peak will shift back to the correct position, as shown in figure 16, and will include a substantial contribution from the low utility signal events from figure 23.

$\tilde{m}_C$ (GeV)	$\tilde{m}_B$ (GeV)	$\tilde{m}_A$ (GeV)
400	505	694
700	800	1000
1000	1098	1304

Table 1. Mass spectrum along the flat direction (A.2) for the three $\tilde{m}_C$ values used in the paper.

arises because there is an additional hidden constraint which is approximately satisfied by events in our sample, but is unaccounted for in our analysis. This constraint arises due to the fact that at LHC energies, the transverse momenta of the parent particles are small relative to their masses. This is a good approximation at hadron colliders like the LHC, provided that the A_i particles are not too light. In this case, one can show that there exists a flat direction near the true mass point which satisfies

$$\frac{d\tilde{m}_A^2}{d\tilde{m}_C^2} = \frac{\tilde{m}_A^2 + \tilde{m}_B^2}{\tilde{m}_C^2 + \tilde{m}_B^2}, \tag{A.1a}$$

$$\frac{d\tilde{m}_B^2}{d\tilde{m}_C^2} = \frac{2\tilde{m}_B^2}{\tilde{m}_C^2 + \tilde{m}_B^2}. \tag{A.1b}$$

These equations can be solved to give

$$\frac{\tilde{m}_A^2 - \tilde{m}_B^2}{\tilde{m}_B} = \frac{m_A^2 - m_B^2}{m_B} = \text{constant}, \tag{A.2a}$$

$$\frac{\tilde{m}_B^2 - \tilde{m}_C^2}{\tilde{m}_B} = \frac{m_B^2 - m_C^2}{m_B} = \text{constant}. \tag{A.2b}$$

Table 1 lists the mass spectrum predicted by (A.2) for the three representative values for $\tilde{m}_C$ used on the plots.

References

[1] J.L. Feng, *Dark matter candidates from particle physics and methods of detection*, *Ann. Rev. Astron. Astrophys.* **48** (2010) 495 [arXiv:1003.0904] [INSPIRE].

[2] D0 collaboration, *Direct measurement of the top quark mass at D0*, *Phys. Rev.* **D 58** (1998) 052001 [hep-ex/9801025] [INSPIRE].

[3] B. Gripaios, K. Sakurai and B. Webber, *Polynomials, Riemann surfaces and reconstructing missing-energy events*, *JHEP* **09** (2011) 140 [arXiv:1103.3438] [INSPIRE].

[4] CMS collaboration, *Measurement of the top quark mass with lepton+jets final states using pp collisions at* $\sqrt{s} = 13$ *TeV*, *Eur. Phys. J.* **C 78** (2018) 891 [arXiv:1805.01428] [INSPIRE].

[5] S.P. Martin, *A supersymmetry primer*, *Adv. Ser. Direct. High Energy Phys.* **18** (1998) 1 [hep-ph/9709356] [INSPIRE].

[6] T. Appelquist, H.-C. Cheng and B.A. Dobrescu, *Bounds on universal extra dimensions*, *Phys. Rev.* **D 64** (2001) 035002 [hep-ph/0012100] [INSPIRE].

[7] T.G. Rizzo, *Probes of universal extra dimensions at colliders*, *Phys. Rev.* **D 64** (2001) 095010 [hep-ph/0106336] [INSPIRE].

[8] H.-C. Cheng, K.T. Matchev and M. Schmaltz, *Bosonic supersymmetry? Getting fooled at the CERN LHC*, *Phys. Rev.* **D 66** (2002) 056006 [hep-ph/0205314] [INSPIRE].

[9] N. Arkani-Hamed, A.G. Cohen, E. Katz and A.E. Nelson, *The Littlest Higgs*, *JHEP* **07** (2002) 034 [hep-ph/0206021] [INSPIRE].

[10] H.-C. Cheng and I. Low, *Little hierarchy, little Higgses and a little symmetry*, *JHEP* **08** (2004) 061 [hep-ph/0405243] [INSPIRE].

[11] M. Schmaltz and D. Tucker-Smith, *Little Higgs review*, *Ann. Rev. Nucl. Part. Sci.* **55** (2005) 229 [hep-ph/0502182] [INSPIRE].

[12] M. Perelstein, *Little Higgs models and their phenomenology*, *Prog. Part. Nucl. Phys.* **58** (2007) 247 [hep-ph/0512128] [INSPIRE].

[13] CMS collaboration, *Measurement of masses in the $t\bar{t}$ system by kinematic endpoints in pp collisions at $\sqrt{s} = 7$ TeV*, *Eur. Phys. J.* **C 73** (2013) 2494 [arXiv:1304.5783] [INSPIRE].

[14] A.J. Barr and C.G. Lester, *A review of the mass measurement techniques proposed for the Large Hadron Collider*, *J. Phys.* **G 37** (2010) 123001 [arXiv:1004.2732] [INSPIRE].

[15] M.M. Nojiri, G. Polesello and D.R. Tovey, *Proposal for a new reconstruction technique for SUSY processes at the LHC*, hep-ph/0312317 [INSPIRE].

[16] K. Kawagoe, M.M. Nojiri and G. Polesello, *A new SUSY mass reconstruction method at the CERN LHC*, *Phys. Rev.* **D 71** (2005) 035008 [hep-ph/0410160] [INSPIRE].

[17] H.-C. Cheng et al., *Mass determination in SUSY-like events with missing energy*, *JHEP* **12** (2007) 076 [arXiv:0707.0030] [INSPIRE].

[18] H.-C. Cheng et al., *Accurate mass determinations in decay chains with missing energy*, *Phys. Rev. Lett.* **100** (2008) 252001 [arXiv:0802.4290] [INSPIRE].

[19] H.-C. Cheng, J.F. Gunion, Z. Han and B. McElrath, *Accurate mass determinations in decay chains with missing energy. II*, *Phys. Rev.* **D 80** (2009) 035020 [arXiv:0905.1344] [INSPIRE].

[20] B. Webber, *Mass determination in sequential particle decay chains*, *JHEP* **09** (2009) 124 [arXiv:0907.5307] [INSPIRE].

[21] M.M. Nojiri, G. Polesello and D.R. Tovey, *A hybrid method for determining SUSY particle masses at the LHC with fully identified cascade decays*, *JHEP* **05** (2008) 014 [arXiv:0712.2718] [INSPIRE].

[22] R.M. Djilkibaev and R.V. Konoplich, *A new approach for reconstructing SUSY particle masses with a few fb^{-1} at the LHC*, *JHEP* **08** (2008) 036 [arXiv:0806.2836] [INSPIRE].

[23] D. Casadei, R. Konoplich and R. Djilkibaev, *Reconstruction of stop quark mass at the LHC*, *Phys. Rev.* **D 82** (2010) 075011 [arXiv:1006.5875] [INSPIRE].

[24] N. Kersting, *A simple mass reconstruction technique for SUSY particles at the LHC*, *Phys. Rev.* **D 79** (2009) 095018 [arXiv:0901.2765] [INSPIRE].

[25] Z. Kang et al., *Neutralino reconstruction at the LHC from decay-frame kinematics*, *Eur. Phys. J.* **C 70** (2010) 271 [arXiv:0908.1550] [INSPIRE].

[26] A.J. Barr et al., *Guide to transverse projections and mass-constraining variables*, *Phys. Rev.* **D 84** (2011) 095031 [arXiv:1105.2977] [INSPIRE].

[27] D. Kim, K.T. Matchev, F. Moortgat and L. Pape, *Testing invisible momentum ansatze in missing energy events at the LHC*, *JHEP* **08** (2017) 102 [arXiv:1703.06887] [INSPIRE].

[28] C.G. Lester and D.J. Summers, *Measuring masses of semiinvisibly decaying particles pair produced at hadron colliders*, *Phys. Lett.* **B 463** (1999) 99 [hep-ph/9906349] [INSPIRE].

[29] A. Barr, C. Lester and P. Stephens, $m(T2)$: *the truth behind the glamour*, *J. Phys.* **G 29** (2003) 2343 [hep-ph/0304226] [INSPIRE].

[30] M. Burns, K. Kong, K.T. Matchev and M. Park, *Using subsystem $m(T2)$ for complete mass determinations in decay chains with missing energy at hadron colliders*, *JHEP* **03** (2009) 143 [arXiv:0810.5576] [INSPIRE].

[31] A.J. Barr, B. Gripaios and C.G. Lester, *Transverse masses and kinematic constraints: from the boundary to the crease*, *JHEP* **11** (2009) 096 [arXiv:0908.3779] [INSPIRE].

[32] P. Konar, K. Kong, K.T. Matchev and M. Park, *Superpartner mass measurement technique using 1D orthogonal decompositions of the Cambridge transverse mass variable m_{T2}*, *Phys. Rev. Lett.* **105** (2010) 051802 [arXiv:0910.3679] [INSPIRE].

[33] P. Konar, K. Kong, K.T. Matchev and M. Park, *Dark matter particle spectroscopy at the LHC: generalizing m_{T2} to asymmetric event topologies*, *JHEP* **04** (2010) 086 [arXiv:0911.4126] [INSPIRE].

[34] P. Konar, K. Kong and K.T. Matchev, $\sqrt{\hat{s}}_{min}$: *a global inclusive variable for determining the mass scale of new physics in events with missing energy at hadron colliders*, *JHEP* **03** (2009) 085 [arXiv:0812.1042] [INSPIRE].

[35] P. Konar, K. Kong, K.T. Matchev and M. Park, *RECO level $\sqrt{s}_{min}$ and subsystem $\sqrt{s}_{min}$: Improved global inclusive variables for measuring the new physics mass scale in E_T events at hadron colliders*, *JHEP* **06** (2011) 041 [arXiv:1006.0653] [INSPIRE].

[36] A.K. Swain and P. Konar, *Constrained $\sqrt{\hat{s}}_{min}$ and reconstructing with semi-invisible production at hadron colliders*, *JHEP* **03** (2015) 142 [arXiv:1412.6624] [INSPIRE].

[37] A.J. Barr, B. Gripaios and C.G. Lester, *Measuring the Higgs boson mass in dileptonic W-boson decays at hadron colliders*, *JHEP* **07** (2009) 072 [arXiv:0902.4864] [INSPIRE].

[38] E. Gross and O. Vitells, *Transverse mass observables for charged Higgs boson searches at hadron colliders*, *Phys. Rev.* **D 81** (2010) 055010 [arXiv:0907.5367] [INSPIRE].

[39] A.J. Barr, S.T. French, J.A. Frost and C.G. Lester, *Speedy Higgs boson discovery in decays to tau lepton pairs: $h \to \tau\tau$*, *JHEP* **10** (2011) 080 [arXiv:1106.2322] [INSPIRE].

[40] A.J. Barr, B. Gripaios and C.G. Lester, *Re-weighing the evidence for a Higgs boson in dileptonic W-boson decays*, *Phys. Rev. Lett.* **108** (2012) 041803 [*Erratum ibid.* **108** (2012) 109902] [arXiv:1108.3468] [INSPIRE].

[41] W.S. Cho, J.E. Kim and J.-H. Kim, *Amplification of endpoint structure for new particle mass measurement at the LHC*, *Phys. Rev.* **D 81** (2010) 095010 [arXiv:0912.2354] [INSPIRE].

[42] W.S. Cho, W. Klemm and M.M. Nojiri, *Mass measurement in boosted decay systems at hadron colliders*, *Phys. Rev.* **D 84** (2011) 035018 [arXiv:1008.0391] [INSPIRE].

[43] G.G. Ross and M. Serna, *Mass determination of new states at hadron colliders*, *Phys. Lett.* **B 665** (2008) 212 [arXiv:0712.0943] [INSPIRE].

[44] A.J. Barr, G.G. Ross and M. Serna, *The precision determination of invisible-particle masses at the LHC*, *Phys. Rev.* **D 78** (2008) 056006 [arXiv:0806.3224] [INSPIRE].

[45] W.S. Cho, K. Choi, Y.G. Kim and C.B. Park, m_{T2}-*assisted on-shell reconstruction of missing momenta and its application to spin measurement at the LHC*, *Phys. Rev.* **D 79** (2009) 031701 [arXiv:0810.4853] [INSPIRE].

[46] K. Choi, S. Choi, J.S. Lee and C.B. Park, *Reconstructing the Higgs boson in dileptonic W decays at hadron collider*, *Phys. Rev.* **D 80** (2009) 073010 [arXiv:0908.0079] [INSPIRE].

[47] C.B. Park, *Reconstructing the heavy resonance at hadron colliders*, *Phys. Rev.* **D 84** (2011) 096001 [arXiv:1106.6087] [INSPIRE].

[48] D. Guadagnoli and C.B. Park, m_{T2}-*reconstructed invisible momenta as spin analizers and an application to top polarization*, *JHEP* **01** (2014) 030 [arXiv:1308.2226] [INSPIRE].

[49] R. Mahbubani, K.T. Matchev and M. Park, *Re-interpreting the Oxbridge stransverse mass variable MT2 in general cases*, *JHEP* **03** (2013) 134 [arXiv:1212.1720] [INSPIRE].

[50] W.S. Cho et al., *On-shell constrained M_2 variables with applications to mass measurements and topology disambiguation*, *JHEP* **08** (2014) 070 [arXiv:1401.1449] [INSPIRE].

[51] W.S. Cho et al., *Improving the sensitivity of stop searches with on-shell constrained invariant mass variables*, *JHEP* **05** (2015) 040 [arXiv:1411.0664] [INSPIRE].

[52] D. Kim, H.-S. Lee and M. Park, *Invisible dark gauge boson search in top decays using a kinematic method*, *JHEP* **03** (2015) 134 [arXiv:1411.0668] [INSPIRE].

[53] W.S. Cho et al., *OPTIMASS: a package for the minimization of kinematic mass functions with constraints*, *JHEP* **01** (2016) 026 [arXiv:1508.00589] [INSPIRE].

[54] P. Konar and A.K. Swain, *Mass reconstruction with M_2 under constraint in semi-invisible production at a hadron collider*, *Phys. Rev.* **D 93** (2016) 015021 [arXiv:1509.00298] [INSPIRE].

[55] P. Konar and A.K. Swain, *Reconstructing semi-invisible events in resonant τ pair production from Higgs*, *Phys. Lett.* **B 757** (2016) 211 [arXiv:1602.00552] [INSPIRE].

[56] D. Gonçalves, K. Kong and J.H. Kim, *Probing the top-Higgs Yukawa CP structure in dileptonic $t\bar{t}h$ with M_2-assisted reconstruction*, *JHEP* **06** (2018) 079 [arXiv:1804.05874] [INSPIRE].

[57] I. Hinchliffe et al., *Precision SUSY measurements at CERN LHC*, *Phys. Rev.* **D 55** (1997) 5520 [hep-ph/9610544] [INSPIRE].

[58] H. Bachacou, I. Hinchliffe and F.E. Paige, *Measurements of masses in SUGRA models at CERN LHC*, *Phys. Rev.* **D 62** (2000) 015009 [hep-ph/9907518] [INSPIRE].

[59] B.C. Allanach, C.G. Lester, M.A. Parker and B.R. Webber, *Measuring sparticle masses in nonuniversal string inspired models at the LHC*, *JHEP* **09** (2000) 004 [hep-ph/0007009] [INSPIRE].

[60] B.K. Gjelsten, D.J. Miller and P. Osland, *Measurement of SUSY masses via cascade decays for SPS 1a*, *JHEP* **12** (2004) 003 [hep-ph/0410303] [INSPIRE].

[61] B.K. Gjelsten, D.J. Miller and P. Osland, *Measurement of the gluino mass via cascade decays for SPS 1a*, *JHEP* **06** (2005) 015 [hep-ph/0501033] [INSPIRE].

[62] K.T. Matchev, F. Moortgat, L. Pape and M. Park, *Precise reconstruction of sparticle masses without ambiguities*, *JHEP* **08** (2009) 104 [arXiv:0906.2417] [INSPIRE].

[63] K.T. Matchev, F. Moortgat and L. Pape, *Dreaming awake: disentangling the underlying physics in case of a SUSY-like discovery at the LHC*, *J. Phys.* **G 46** (2019) 115002 [arXiv:1902.11267] [INSPIRE].

[64] K. Agashe, D. Kim, D.G.E. Walker and L. Zhu, *Using m_{T2} to distinguish dark matter stabilization symmetries*, *Phys. Rev.* **D 84** (2011) 055020 [arXiv:1012.4460] [INSPIRE].

[65] D. Curtin, *Mixing it up with m_{T2}: unbiased mass measurements at hadron colliders*, *Phys. Rev.* **D 85** (2012) 075004 [arXiv:1112.1095] [INSPIRE].

[66] H.-C. Cheng and Z. Han, *Minimal kinematic constraints and m_{T2}*, *JHEP* **12** (2008) 063 [arXiv:0810.5178] [INSPIRE].

[67] G. Anagnostou, *Model independent search in 2-dimensional mass space*, *EPJ Web Conf.* **71** (2014) 00006 [arXiv:1112.3379] [INSPIRE].

[68] I.-W. Kim, *Algebraic singularity method for mass measurement with missing energy*, *Phys. Rev. Lett.* **104** (2010) 081601 [arXiv:0910.1149] [INSPIRE].

[69] J.L. Feng and T. Moroi, *Supernatural supersymmetry: phenomenological implications of anomaly mediated supersymmetry breaking*, *Phys. Rev.* **D 61** (2000) 095004 [hep-ph/9907319] [INSPIRE].

[70] J.L. Feng, K.T. Matchev and T. Moroi, *Focus points and naturalness in supersymmetry*, *Phys. Rev.* **D 61** (2000) 075005 [hep-ph/9909334] [INSPIRE].

[71] C.G. Lester, *Mass and spin measurement techniques (for the Large Hadron Collider)*, lectures given at *Theoretical Advanced Study Institute in Elementary Particle Physics: The Dark Secrets of the Terascale (TASI 2011)*, June 6–July 1, Boulder, U.S.A. (2011).

[72] P. Agrawal, C. Kilic, C. White and J.-H. Yu, *Improved mass measurement using the boundary of many-body phase space*, *Phys. Rev.* **D 89** (2014) 015021 [arXiv:1308.6560] [INSPIRE].

[73] D. Debnath et al., *Detecting kinematic boundary surfaces in phase space: particle mass measurements in SUSY-like events*, *JHEP* **06** (2017) 092 [arXiv:1611.04487] [INSPIRE].

[74] B. Altunkaynak, C. Kilic and M.D. Klimek, *Multidimensional phase space methods for mass measurements and decay topology determination*, *Eur. Phys. J.* **C 77** (2017) 61 [arXiv:1611.09764] [INSPIRE].

[75] D. Debnath et al., *Enhancing the discovery prospects for SUSY-like decays with a forgotten kinematic variable*, *JHEP* **05** (2019) 008 [arXiv:1809.04517] [INSPIRE].

[76] P. Baringer, K. Kong, M. McCaskey and D. Noonan, *Revisiting combinatorial ambiguities at hadron colliders with m_{T2}*, *JHEP* **10** (2011) 101 [arXiv:1109.1563] [INSPIRE].

[77] K. Choi, D. Guadagnoli and C.B. Park, *Reducing combinatorial uncertainties: a new technique based on m_{T2} variables*, *JHEP* **11** (2011) 117 [arXiv:1109.2201] [INSPIRE].

[78] D. Debnath et al., *Resolving combinatorial ambiguities in dilepton $t\bar{t}$ event topologies with constrained M_2 variables*, *Phys. Rev.* **D 96** (2017) 076005 [arXiv:1706.04995] [INSPIRE].

[79] Y. Grossman, M. Martone and D.J. Robinson, *Kinematic edges with flavor oscillation and non-zero widths*, *JHEP* **10** (2011) 127 [arXiv:1108.5381] [INSPIRE].

[80] D. Kim and K.T. Matchev, *How to prove that a E_T excess at the LHC is not due to dark matter*, *Phys. Rev.* **D 98** (2018) 055018 [arXiv:1712.07620] [INSPIRE].

[81] J. Alwall et al., *MadGraph 5: going beyond*, *JHEP* **06** (2011) 128 [arXiv:1106.0522] [INSPIRE].

[82] L. Sonnenschein, *Algebraic approach to solve* $t\bar{t}$ *dilepton equations*, *Phys. Rev.* **D 72** (2005) 095020 [`hep-ph/0510100`] [INSPIRE].

[83] L. Sonnenschein, *Analytical solution of* $t\bar{t}$ *dilepton equations*, *Phys. Rev.* **D 73** (2006) 054015 [*Erratum ibid.* **D 78** (2008) 079902] [`hep-ph/0603011`] [INSPIRE].

[84] B.A. Betchart, R. Demina and A. Harel, *Analytic solutions for neutrino momenta in decay of top quarks*, *Nucl. Instrum. Meth.* **A 736** (2014) 169 [`arXiv:1305.1878`] [INSPIRE].

[85] W.S. Cho, K. Choi, Y.G. Kim and C.B. Park, *Gluino stransverse mass*, *Phys. Rev. Lett.* **100** (2008) 171801 [`arXiv:0709.0288`] [INSPIRE].

[86] A.J. Barr, B. Gripaios and C.G. Lester, *Weighing Wimps with kinks at colliders: invisible particle mass measurements from endpoints*, *JHEP* **02** (2008) 014 [`arXiv:0711.4008`] [INSPIRE].

[87] W.S. Cho, K. Choi, Y.G. Kim and C.B. Park, *Measuring superparticle masses at hadron collider using the transverse mass kink*, *JHEP* **02** (2008) 035 [`arXiv:0711.4526`] [INSPIRE].

[88] K.T. Matchev, F. Moortgat, L. Pape and M. Park, *Precision sparticle spectroscopy in the inclusive same-sign dilepton channel at LHC*, *Phys. Rev.* **D 82** (2010) 077701 [`arXiv:0909.4300`] [INSPIRE].

[89] K.T. Matchev and M. Park, *A general method for determining the masses of semi-invisibly decaying particles at hadron colliders*, *Phys. Rev. Lett.* **107** (2011) 061801 [`arXiv:0910.1584`] [INSPIRE].

[90] B. Gripaios, *Transverse observables and mass determination at hadron colliders*, *JHEP* **02** (2008) 053 [`arXiv:0709.2740`] [INSPIRE].

[91] A. Betancur et al., *Measuring the mass, width and couplings of semi-invisible resonances with the matrix element method*, *Phys. Rev.* **D 99** (2019) 116007 [`arXiv:1708.07641`] [INSPIRE].

[92] CMS collaboration, *Jet energy scale and resolution in the CMS experiment in pp collisions at 8 TeV*, 2017 *JINST* **12** P02014 [`arXiv:1607.03663`] [INSPIRE].